A stepwise neuron model fitting procedure designed for recordings with high spatial resolution: application to layer 5 pyramidal cells — Supplementary material

September 7, 2017

S1 Parameter value ranges

The parameter value ranges shown in Table 1 are taken from Table 2 in [S1], with the following exceptions. The upper bound for the leak conductances are double the values given in [S1]. The I_h conductances, which were not fitted in [S1], are limited between 0 and approximately eight-fold value of the maximal conductance of [S1]. The upper limits for $CaHVA$ and $CaLVA$ conductances in the apical tuft are ten-fold compared to those in [S1] — this is done to make it possible for the model to capture the contribution of the "hot zone" of Ca^{2+} channels. For the compartment lengths, the ranges of possible values are from half to double the corresponding (maximal) compartment lengths in cell #1 of [S1] (note that the apical dendrite is divided into two compartments). The values of axial resistances are limited to five-fold changes from the original value (100 Ωcm) in the soma and ten-fold changes elsewhere. For membrane capacitances at the soma, two-fold changes from the original value (1.0 µF/cm^2) are allowed. In [S1], the membrane capacitances at the dendrites were doubled (2.0 µF/cm^2) in order to capture the effect of dendritic spines: here, we set the range of possible values from 0.5 µF/cm^2 to 2.0 µF/cm^2.

S2 Fitting the third step parameters using an additional compartment to describe the hot zone of Ca^{2+} channels

Here, we show that the quality of the fit at the third step could be improved by allowing a hot zone of Ca^{2+} channels inside what previously was the compartment representing the apical tuft. We used the first and second step model parameters as obtained in Figure 1–2 (see Table 3), and divided the distal apical compartment into three sections, of which the first and third have the same Ca^{2+} conductances, while the HVA Ca^{2+} conductances of the middle section were multiplied by a factor from 1 to 20 (10 in the original Hay model) and the LVA Ca^{2+} conductances by a factor from 1 to 200 (100 in the original Hay model). Figure S1 shows fitting results obtained with this scheme, and Table S1 shows the obtained paramater values. The obtained model fitted better to the Ca^{2+} concentration data along the apical dendrite, especially for the responses to large-amplitude apical stimuli (objectives 3.4b and 3.5b) that were underestimated in the standard four-compartment model. Note that also the amplitudes of the responses at the dendrites to other stimuli of objectives 3.2–3.5 were better fitted by eye, although this was not always captured by the error function — to gain a better fit, the error function (Equation 5) could be refined to give larger error values to responses of too small amplitudes. The time course of the somatic membrane potential (objective 3.1) shows a slightly worse fit than in the standard model. However, choosing another parameter set from the Pareto-front would give a better fit for objective 3.1, at the expense of the fit of the spatial distribution of membrane potential and Ca^{2+} concentration (objectives 3.2–3.5). In the obtained parameter set, the Ca^{2+} dynamics were faster in the apical dendrite than in the standard four-compartment model where the hot zone was not included (Table 3). While both HVA and LVA Ca^{2+} channel conductances were zero in the apical trunk in the four-compartment model, here all Ca^{2+} channel conductance were non-zero. The SK conductances were very similar between the two (except in the apical trunk, where the SK channels played no role in the four-compartment model as the Ca^{2+} inputs to the underlying compartment were zero).
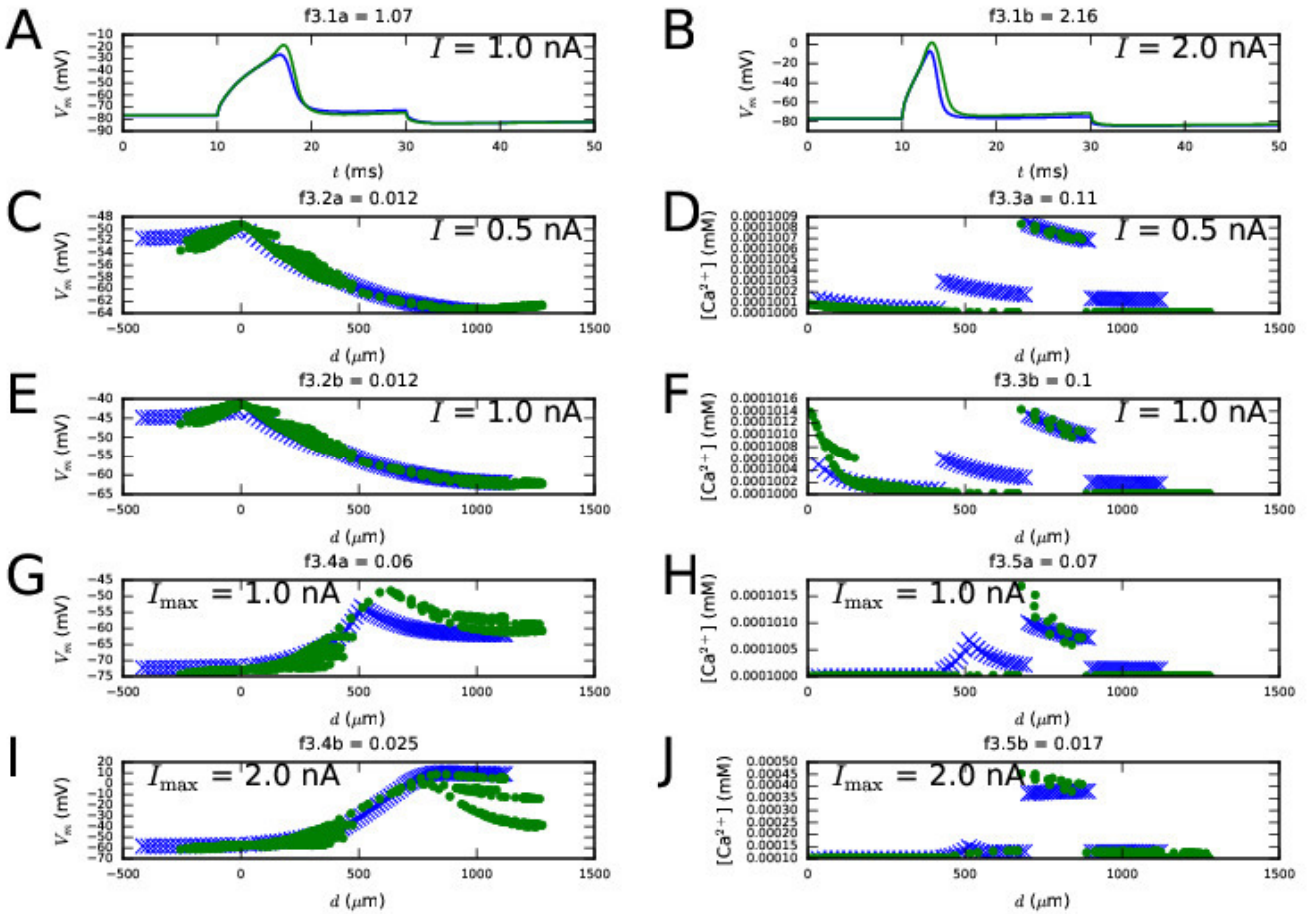

Figure S1: **Third step fit using the scheme where an additional compartment with a hot zone of Ca^{2+} channels is included**. See Figure 3 for details.

Table S1: **Parameter values from third step fitting including the hot zone of Ca^{2+} channels**.

Variable	Value
$g_{\text{CaHVA}}^{\text{soma}}$	0.000419
$g_{\text{CaLVA}}^{\text{soma}}$	0.000628
γ^{soma}	0.00174
$\tau\text{decay}^{\text{soma}}$	586
$g_{\text{SK}}^{\text{soma}}$	0.0533
$g_{\text{CaHVA}}^{\text{apic}}$	$7.79 \cdot 10^{-5}$
$g_{\text{CaLVA}}^{\text{apic}}$	0.00139
γ^{apic}	0.00103
$\tau\text{decay}^{\text{apic}}$	21.3
$g_{\text{SK}}^{\text{apic}}$	0.000994
$g_{\text{CaHVA}}^{\text{tuft}}$	$7.62 \cdot 10^{-5}$
$g_{\text{CaLVA}}^{\text{tuft}}$	0.0239
γ^{tuft}	0.0005
$\tau\text{decay}^{\text{tuft}}$	20
$g_{\text{SK}}^{\text{tuft}}$	0.00336
$c_{\text{hot zone coefficient, HVA}}$	13.7
$c_{\text{hot zone coefficient, LVA}}$	4.91

S3   Fitting all parameters simultaneously

The stepwise method we developed benefits both from the fact that the parameter space is smaller and from the fact that the objective functions at each step quantify the error under circumstances where the fitted conductances play a large role, i.e., when other, typically faster ion channels are blocked. In this section, we aim to show that fitting the parameters of all four steps in a single optimization task using objective functions that only quantify the intact neuron behaviour (i.e., without ion-channel blockers) is less likely to succeed than the stepwise fitting protocol. We used the objective functions of the last step, but also included the distribution of membrane potential and calcium concentration across the dendrites in a similar fashion as in the objective functions of the third step. However, we modified the amplitudes of the stimuli of the third step objectives such that no somatic spikes were initiated. The objective functions are given in Table S2.

Table S2: **Objective functions used when all model parameters are fitted simultaneously**. The first column shows the objective number, and the corresponding objective number in the stepwise method is given in parenthesis. See Table 2 for details.

Objective number	Objective function	Where measured	Stimulus type	Eq.	Stimulus amplitude
1(3.2)	Difference in distribution of steady-state membrane potentials	Dendrites	3000-ms DC pulse at soma	(5)	0.15 nA 0.3 nA
2(3.3)	Difference in distribution of steady-state intracellular [Ca^{2+}]	Apical dendrite	3000-ms DC pulse at soma	(5)	0.15 nA 0.3 nA
3(3.4)	Difference in distribution of peak membrane potential	Dendrites	EPSP-like current injection at the apical dendrite 620 µm from soma	(5)	0.6 nA 1.2 nA
4(3.5)	Difference in distribution of peak intracellular [Ca^{2+}]	Apical dendrite	EPSP-like current injection at the apical dendrite 620 µm from soma	(5)	0.6 nA 1.2 nA
5(4.1)	Difference in membrane potential time series and numbers of spikes	Soma	100-ms DC pulse at soma	(4)	0.25 nA 0.5 nA
6(4.2)	Difference in membrane potential time series and numbers of spikes	Soma	5-ms DC at soma	(4)	1.9 nA
7(4.3)	Difference in membrane potential time series and numbers of spikes	Soma	5-ms DC at soma and EPSP-like current at apical dendrite	(4)	1.9 nA (soma) + 0.5 nA (apical)
8(4.4)	Difference in numbers of spikes	Soma	3000-ms DC at soma	(3)	0.78 nA 1.0 nA 1.9 nA

We performed the fitting using a population of N_{samp}=2000 samples, N_{gen}=20–29 generations. Out of ten independent fittings with different random number seeds, only one gave parameter sets that resulted in both correct numbers of spikes for objectives 4.1–4.3 and small differences (Equation 3 resulting in a value less than 100) between the f-I curves. The best fit obtained with these parameter sets is illustrated in Figure 6, and the model parameter values are given in Table S3.

Table S3: **Parameter values obtained from the multi-objective optimizations of Figure 6**. See Table 3 for the corresponding parameter values obtained from the stepwise optimizations.

Variable	Value	Variable	Value	Variable	Value	Variable	Value
L^{soma}	32.6	g_l^{soma}	$5.44{\cdot}10^{-5}$	$g_{\text{CaHVA}}^{\text{soma}}$	0.000609	$g_{\text{Nat}}^{\text{soma}}$	2.71
L^{basal}	309	g_l^{basal}	$5.64{\cdot}10^{-5}$	$g_{\text{CaLVA}}^{\text{soma}}$	0.00365	$g_{\text{Nap}}^{\text{soma}}$	0.00833
L^{apic}	642	g_l^{apic}	$7.52{\cdot}10^{-5}$	γ^{soma}	0.0005	$g_{\text{Kt}}^{\text{soma}}$	0.0499
L^{tuft}	945	g_l^{tuft}	$4.1{\cdot}10^{-5}$	$\tau\text{decay}^{\text{soma}}$	715	$g_{\text{Kp}}^{\text{soma}}$	0.0647
R_a^{soma}	62.4	E_h	-53.8	$g_{\text{SK}}^{\text{soma}}$	0.0251	$g_{Kv3.1}^{\text{soma}}$	0.734
R_a^{basal}	931	g_h^{soma}	0.000219	$g_{\text{CaHVA}}^{\text{apic}}$	0.00141	g_m^{apic}	0.000445
R_a^{apic}	528	g_h^{basal}	0.000452	$g_{\text{CaLVA}}^{\text{apic}}$	0.011	$g_{\text{Nat}}^{\text{apic}}$	0.0154
R_a^{tuft}	537	g_h^{apic}	0.00107	γ^{apic}	0.0462	$g_{Kv3.1}^{\text{apic}}$	0.00852
c_m^{soma}	0.877	g_h^{tuft}	0.00444	$\tau\text{decay}^{\text{apic}}$	22.5	g_m^{apic}	0.000239
c_m^{basal}	2.46			$g_{\text{SK}}^{\text{apic}}$	0	$g_{\text{Nat}}^{\text{tuft}}$	0.00895
c_m^{apic}	2.57			$g_{\text{CaHVA}}^{\text{tuft}}$	0.00615	$g_{Kv3.1}^{\text{tuft}}$	0.00762
c_m^{tuft}	2.22			$g_{\text{CaLVA}}^{\text{tuft}}$	0.212		
				γ^{tuft}	0.0493		
				$\tau\text{decay}^{\text{tuft}}$	61.4		
				$g_{\text{SK}}^{\text{tuft}}$	0.0037		

S4 Fitting the model parameters using indicator-based evolutionary algorithm (IBEA)

There is evidence that algorithms using IBEA selection [S2] may outperform NSGA-type algorithms in neuron model fitting tasks [S3] as well as other optimization problems [S4]. Therefore, it can be questioned whether fitting all parameters simultaneously, as done in Section S3, could outperform our four-step fitting scheme if a more suitable genetic algorithm was used. Here, we repeated the experiments of Section S3 using the Platypus implementation of IBEA (https://github.com/Project-Platypus/Platypus, Copyright David Hadka) as the optimization algorithm. We performed the fitting using a population of N_{samp}=2000 samples, N_{gen}=44–57 generations. Only three out of fifteen repetitions of the fitting gave parameter sets that resulted in both correct numbers of spikes for objectives 4.1–4.3 of Table S2 and small differences (Equation 3 resulting in a value less than 100) between the f-I curves. In two of these result sets, the best solutions were characterized by AHP amplitudes that were radically different from those of the target neuron and relatively large differences in f-I curves (data not shown). However, one of the result sets had acceptable solutions, the best one of which is illustrated in Figure S2, and the corresponding model parameter values are given in Table S4. Similarly to the best solution of the single-shot NSGA algorithm (Figure 6 and Table S3), the solution shown in Figure S2 suffers from a mismatch in membrane potential time series between target and fitted data especially when subthreshold stimulus was used (Figure 6I and S2I). The IBEA-based solution was more accurate than then NSGA-based solution in reproducing the membrane potential and Ca^{2+} concentration distributions along the dendrites as well as the f-I curve, but less accurate in reproducing the spike shapes and timings in response to short (<100 ms) stimuli. We conclude that in our single-shot parameter estimation scheme, the IBEA algorithm performed approximately as well as the NSGA algorithm.

Table S4: **Parameter values obtained from the multi-objective optimizations of Figure S2**.

Variable	Value	Variable	Value	Variable	Value	Variable	Value
L^{soma}	27.4	g_l^{soma}	4.33e-05	$g_{\text{CaHVA}}^{\text{soma}}$	0.000413	$g_{\text{Nat}}^{\text{soma}}$	3.5
L^{basal}	553	g_l^{basal}	5.26e-05	$g_{\text{CaLVA}}^{\text{soma}}$	0.000379	$g_{\text{Nap}}^{\text{soma}}$	0.00553
L^{apic}	551	g_l^{apic}	2.83e-05	γ^{soma}	0.00267	$g_{\text{Kt}}^{\text{soma}}$	0.0227
L^{tuft}	623	g_l^{tuft}	2.01e-05	$\tau\text{decay}^{\text{soma}}$	440	$g_{\text{Kp}}^{\text{soma}}$	0.0852
R_a^{soma}	81.7	E_h	-53.8	$g_{\text{SK}}^{\text{soma}}$	0.0209	$g_{Kv3.1}^{\text{soma}}$	1.56
R_a^{basal}	199	g_h^{soma}	0.000601	$g_{\text{CaHVA}}^{\text{apic}}$	0.00015	g_m^{apic}	4.68e-05
R_a^{apic}	408	g_h^{basal}	0.000218	$g_{\text{CaLVA}}^{\text{apic}}$	0.00207	$g_{\text{Nat}}^{\text{apic}}$	0.0189
R_a^{tuft}	419	g_h^{apic}	0.00135	γ^{apic}	0.000784	$g_{Kv3.1}^{\text{apic}}$	0.014
c_m^{soma}	0.611	g_h^{tuft}	0.00127	$\tau\text{decay}^{\text{apic}}$	62.4	g_m^{apic}	1.76e-05
c_m^{basal}	1.01			$g_{\text{SK}}^{\text{apic}}$	0.00103	$g_{\text{Nat}}^{\text{tuft}}$	0.00758
c_m^{apic}	2.24			$g_{\text{CaHVA}}^{\text{tuft}}$	0.00125	$g_{Kv3.1}^{\text{tuft}}$	0.0136
c_m^{tuft}	3.25			$g_{\text{CaLVA}}^{\text{tuft}}$	0.00379		
				γ^{tuft}	0.00387		
				$\tau\text{decay}^{\text{tuft}}$	142		
				$g_{\text{SK}}^{\text{tuft}}$	0.00215		

To show that the success of our four-step method is not strictly dependent on the type of genetic algorithm used, we repeated the default fitting task using the abovementioned IBEA algorithm. Figures S3–S6 show that the IBEA algorithm
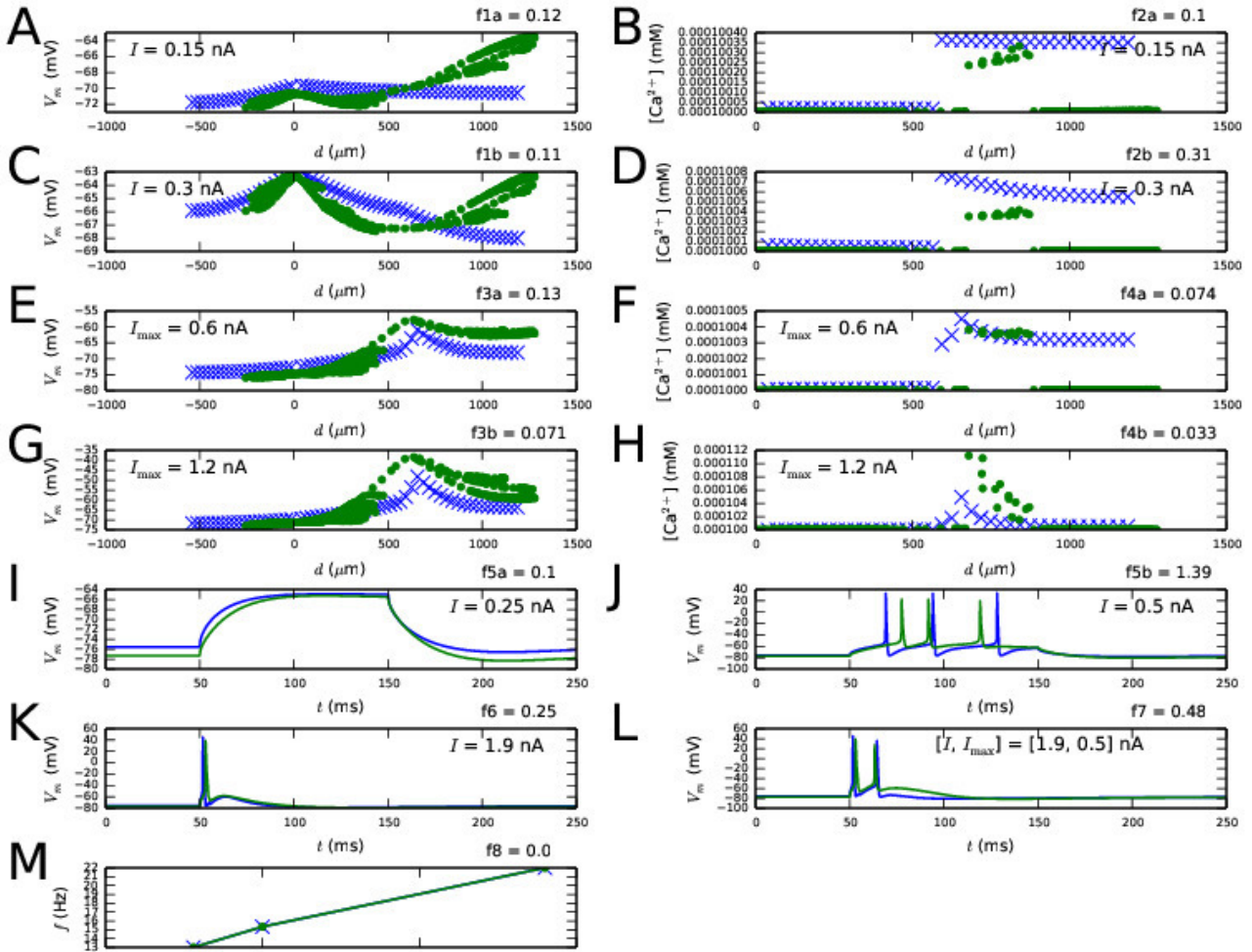
Figure S2: **Results from the experiment where all parameters model parameters were simultaneously fitted using IBEA algorithm**. See Table S2 for the objective functions and Figure 6 for the results from the corresponding NSGA optimization. The parameter values are given in Table S4.

produced a good fit for all four steps. The model parameter values corresponding to the fitted model are shown in Table S5.
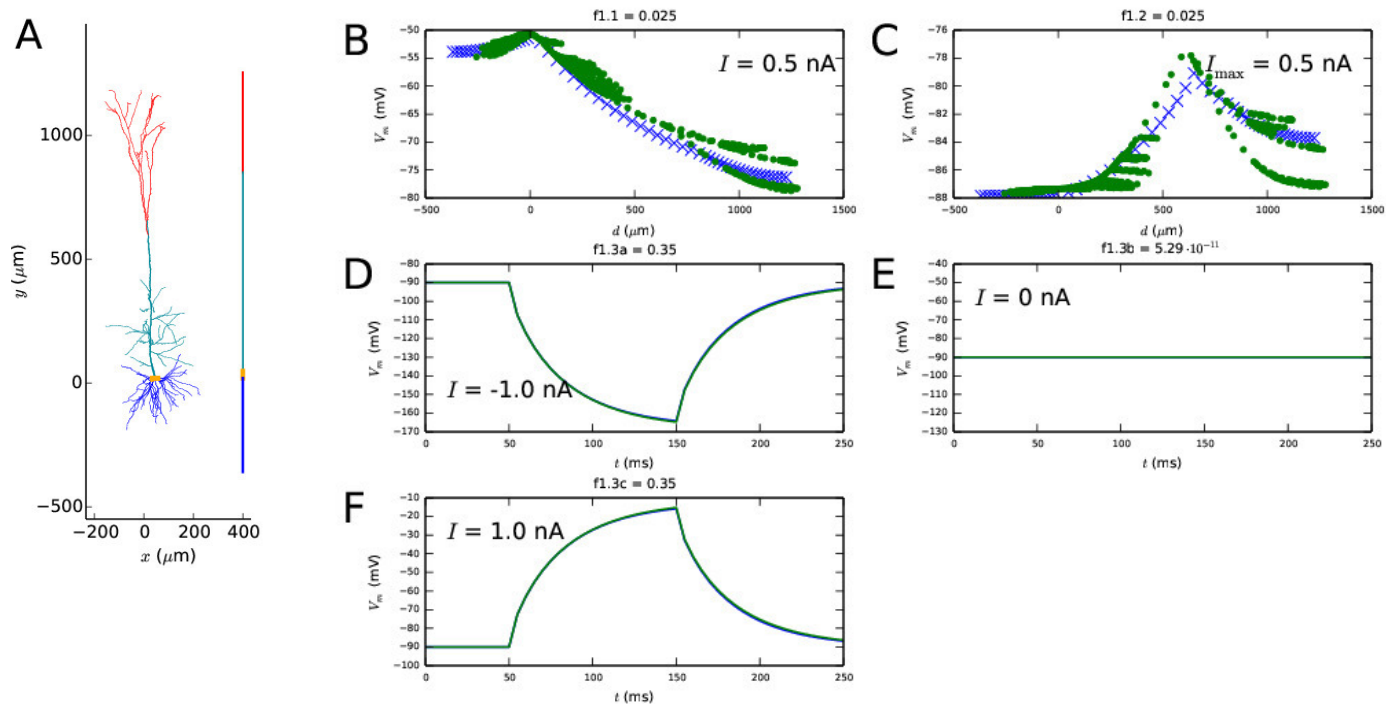

Figure S3: **First step fit using the IBEA algorithm**. See Figure 1 for the corresponding results obtained with NSGA algorithm.
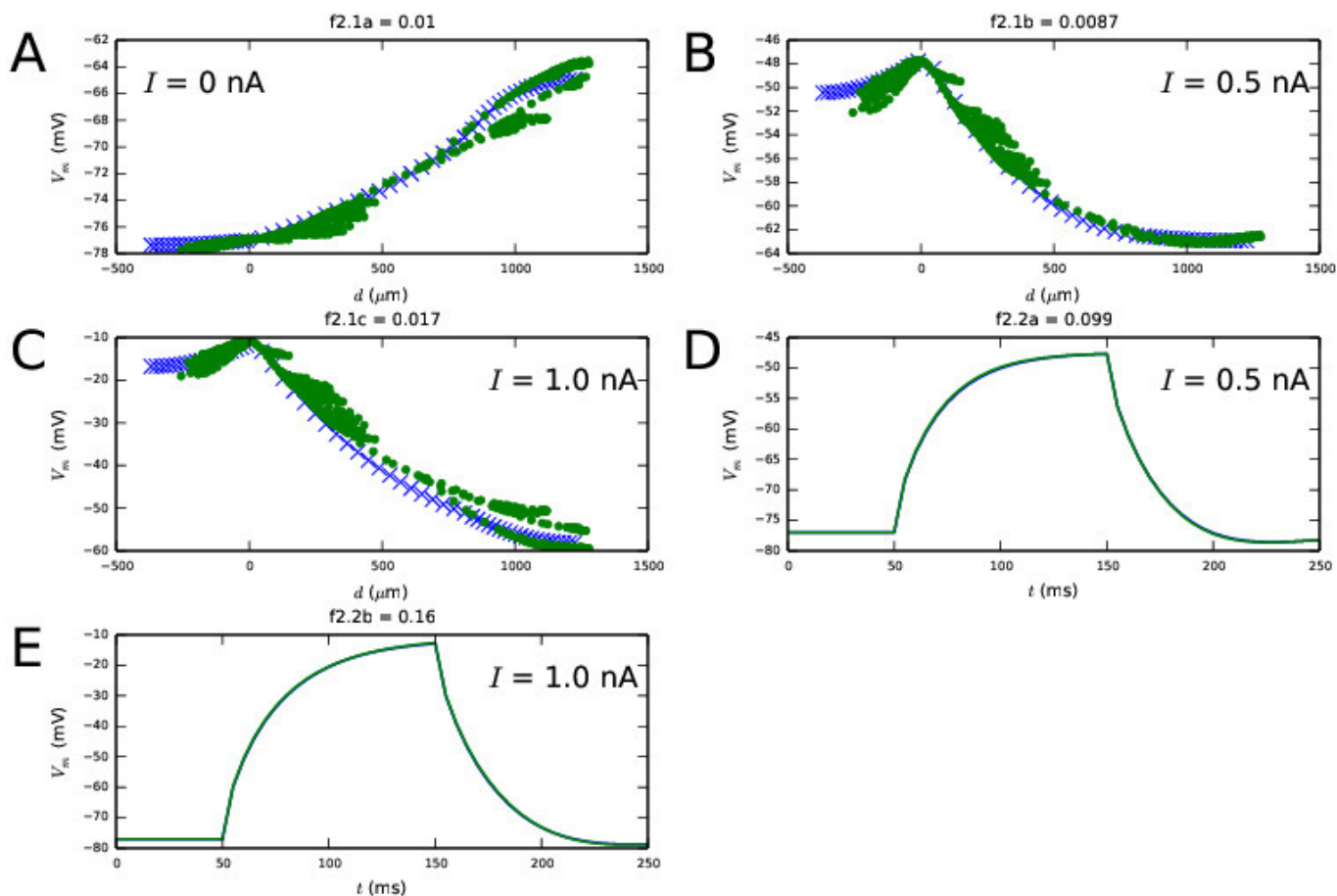
Figure S4: **Second step fit using the IBEA algorithm**. See Figure 2.
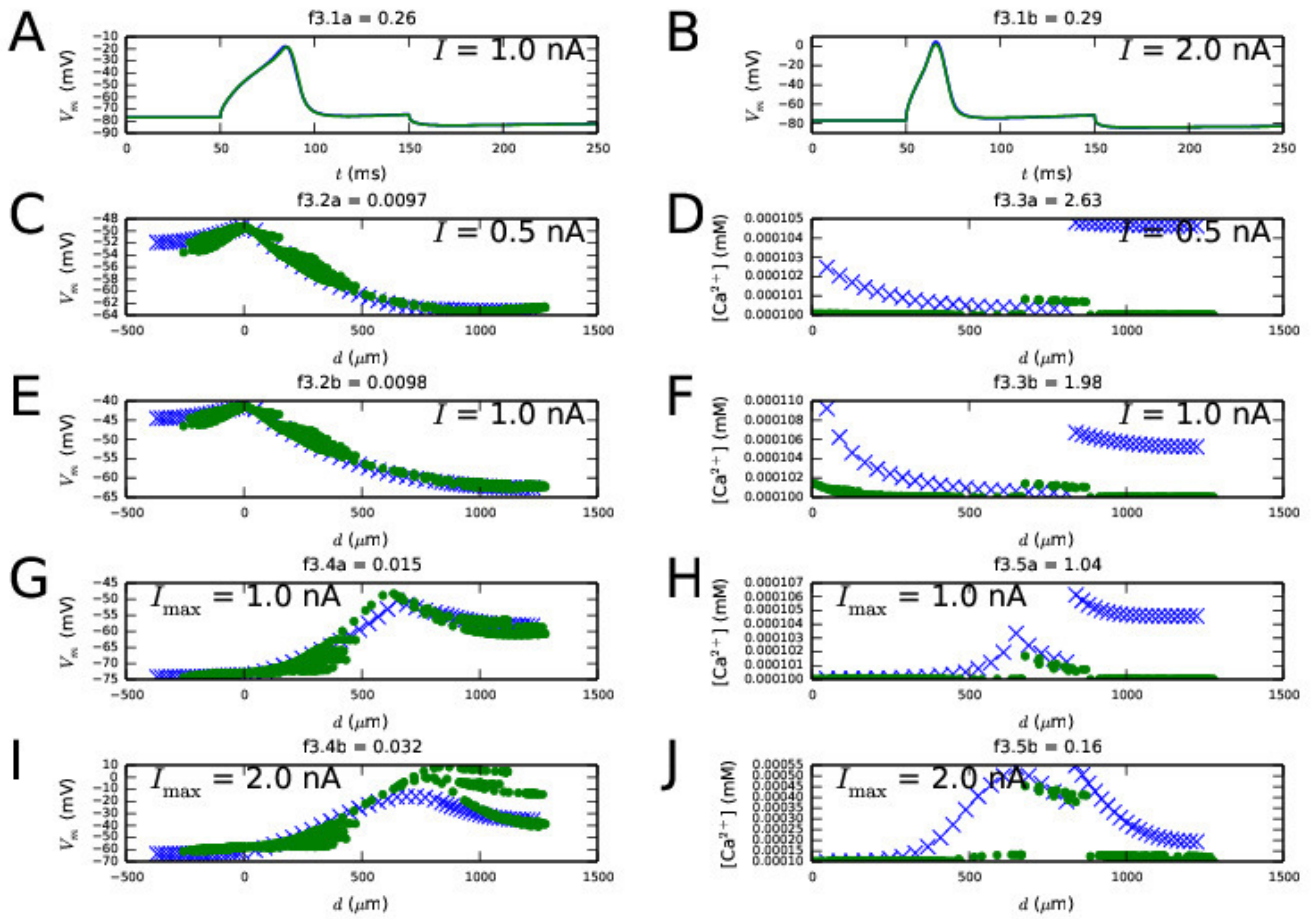
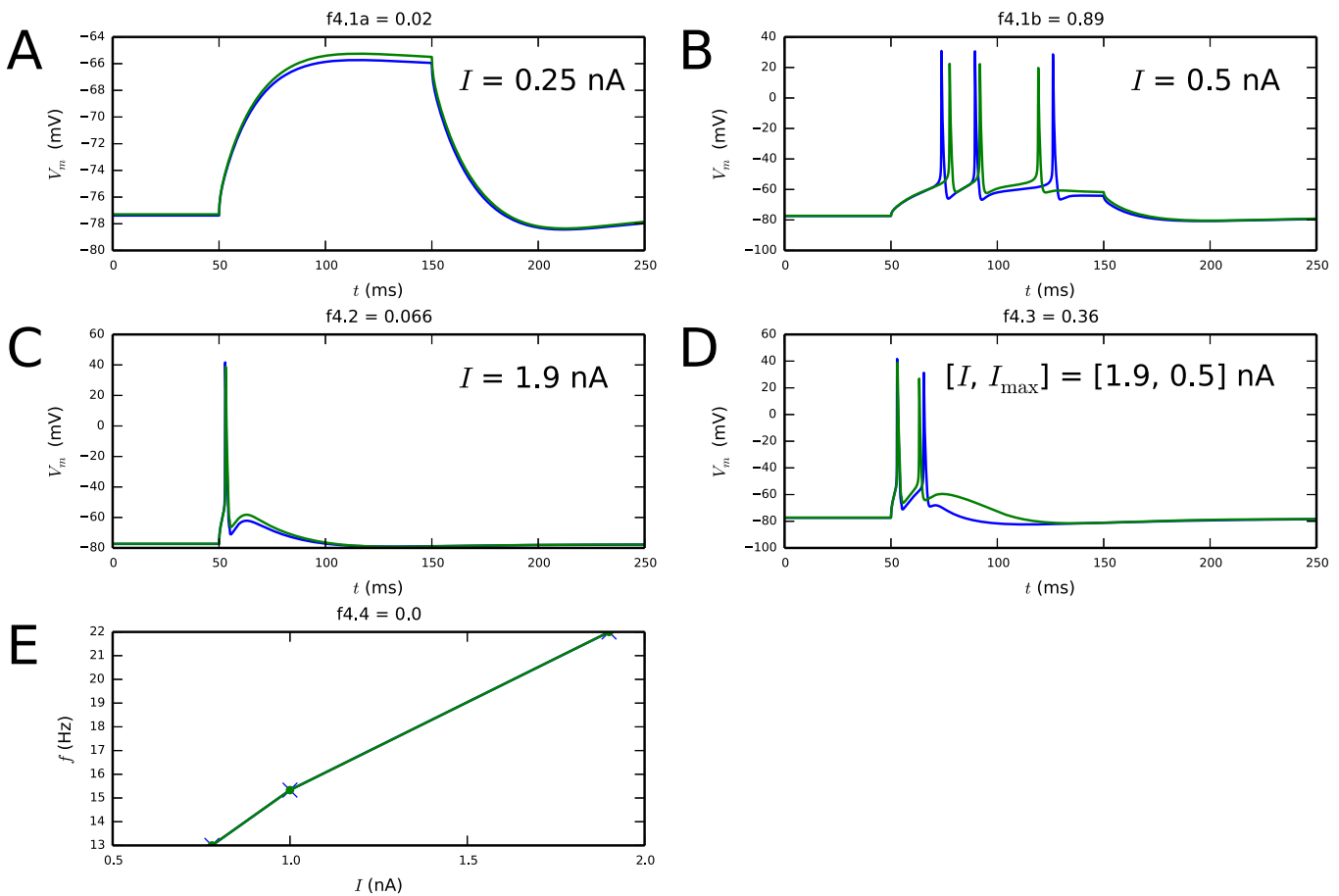Figure S5: **Third step fit using the IBEA algorithm**. See Figure 3.

Figure S6: **Fourth step fit using the IBEA algorithm**. See Figure 4.

Table S5: **Parameter values obtained from the multi-objective optimizations of Figures S3–S6**. See Table 3 for the corresponding parameter values obtained with NSGA algorithm.

STEP 1		STEP 2		STEP 3		STEP 4	
Variable	Value	Variable	Value	Variable	Value	Variable	Value
L^{soma}	29.8	E_h	-48.9	$g_{\text{CaHVA}}^{\text{soma}}$	0.000837	$g_{\text{Nat}}^{\text{soma}}$	2.24
L^{basal}	420	g_h^{soma}	0.000678	$g_{\text{CaLVA}}^{\text{soma}}$	0.000896	$g_{\text{Nap}}^{\text{soma}}$	0.000295
L^{apic}	451	g_h^{basal}	0.000184	γ^{soma}	0.0005	$g_{\text{Kt}}^{\text{soma}}$	0.0515
L^{tuft}	976	g_h^{apic}	0	$\tau\text{decay}^{\text{soma}}$	527	$g_{\text{Kp}}^{\text{soma}}$	0
R_a^{soma}	460	g_h^{tuft}	0.0094	$g_{\text{SK}}^{\text{soma}}$	0.0506	$g_{Kv3.1}^{\text{soma}}$	0.616
R_a^{basal}	172	g_l^{soma}	$3.16 \cdot 10^{-5}$	$g_{\text{CaHVA}}^{\text{apic}}$	0	g_m^{apic}	0.0005
R_a^{apic}	925	g_l^{basal}	$4.42 \cdot 10^{-5}$	$g_{\text{CaLVA}}^{\text{apic}}$	0.00678	$g_{\text{Nat}}^{\text{apic}}$	0.00863
R_a^{tuft}	104	g_l^{apic}	$4.87 \cdot 10^{-5}$	γ^{apic}	0.00365	$g_{Kv3.1}^{\text{apic}}$	0.0119
c_m^{soma}	1.26	g_l^{tuft}	$5.36 \cdot 10^{-5}$	$\tau\text{decay}^{\text{apic}}$	58	g_m^{apic}	0.000188
c_m^{basal}	2.35			$g_{\text{SK}}^{\text{apic}}$	0	$g_{\text{Nat}}^{\text{tuft}}$	0.00819
c_m^{apic}	1.29			$g_{\text{CaHVA}}^{\text{tuft}}$	0.0111	$g_{Kv3.1}^{\text{tuft}}$	0.0109
c_m^{tuft}	2.65			$g_{\text{CaLVA}}^{\text{tuft}}$	0.0185		
				γ^{tuft}	0.043		
				$\tau\text{decay}^{\text{tuft}}$	21		
				$g_{\text{SK}}^{\text{tuft}}$	0.00418		

S5 Model fitting can be carried out using noisy measurements along the dendrites

In experimental recordings, patch-clamp as well as current-clamp data are usually relatively accurate, while the data from VSD measurements are subject to higher levels of noise. We tested the performance of our fitting method using the objective functions of Table 2, but adding a small (SD 1 mV), medium (SD 2 mV), or large (SD 5 mV) Gaussian noise component to all membrane potential values measured along the dendrites. Similarly, all Ca^{2+} concentration values were multiplied by a log-normal noise component $\exp(\mathcal{N}(0, \sigma))$ with small ($\sigma = 0.05$), medium ($\sigma = 0.1$), or large ($\sigma = 0.2$) variance. By contrast, the membrane-potential data at soma were kept accurate. The fitting was carried out to five independently (different random number seeds) generated data sets of each of the three levels of noise. For each level of noise, at least one parameter set that produced an acceptable fit was obtained. Figures S7, S8, S9, and S10 illustrate the fits of the best parameter set (see Table S6) obtained using a large noise in dendritic measurements during each step. Figures S7–S9 show that the noise in dendritic membrane potential and Ca^{2+} concentration data did not invalidate the fit to the data, and Figure S10 shows that the previously obtained parameters for leak, I_h, Ca^{2+} and SK channel conductances allowed the rest of the parameters (Na^+ and K^+ channel conductances) to be fitted to the data such that the correct spiking behavior (including the BAC firing) was reproduced.
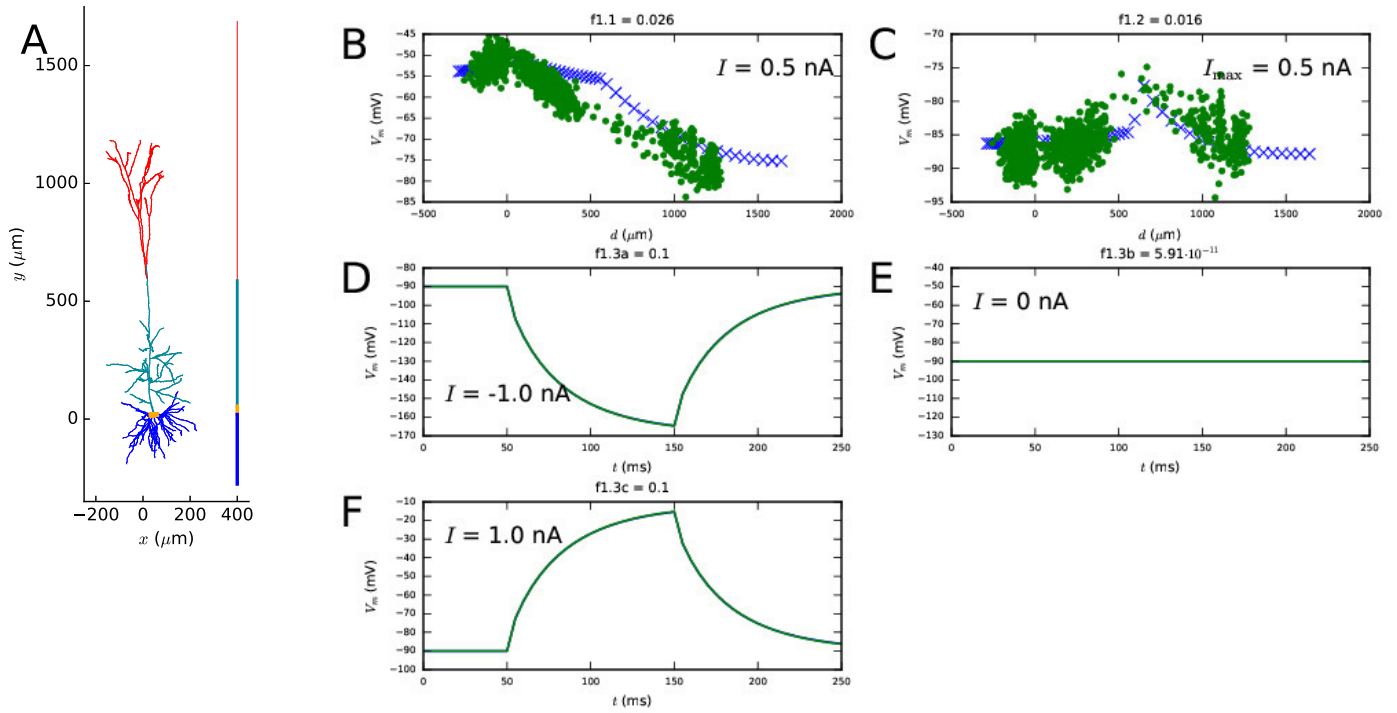
Figure S7: **First step fit using noisy dendritic measurements**. See Figure 1 for the corresponding figure illustrating fitting to noiseless data.
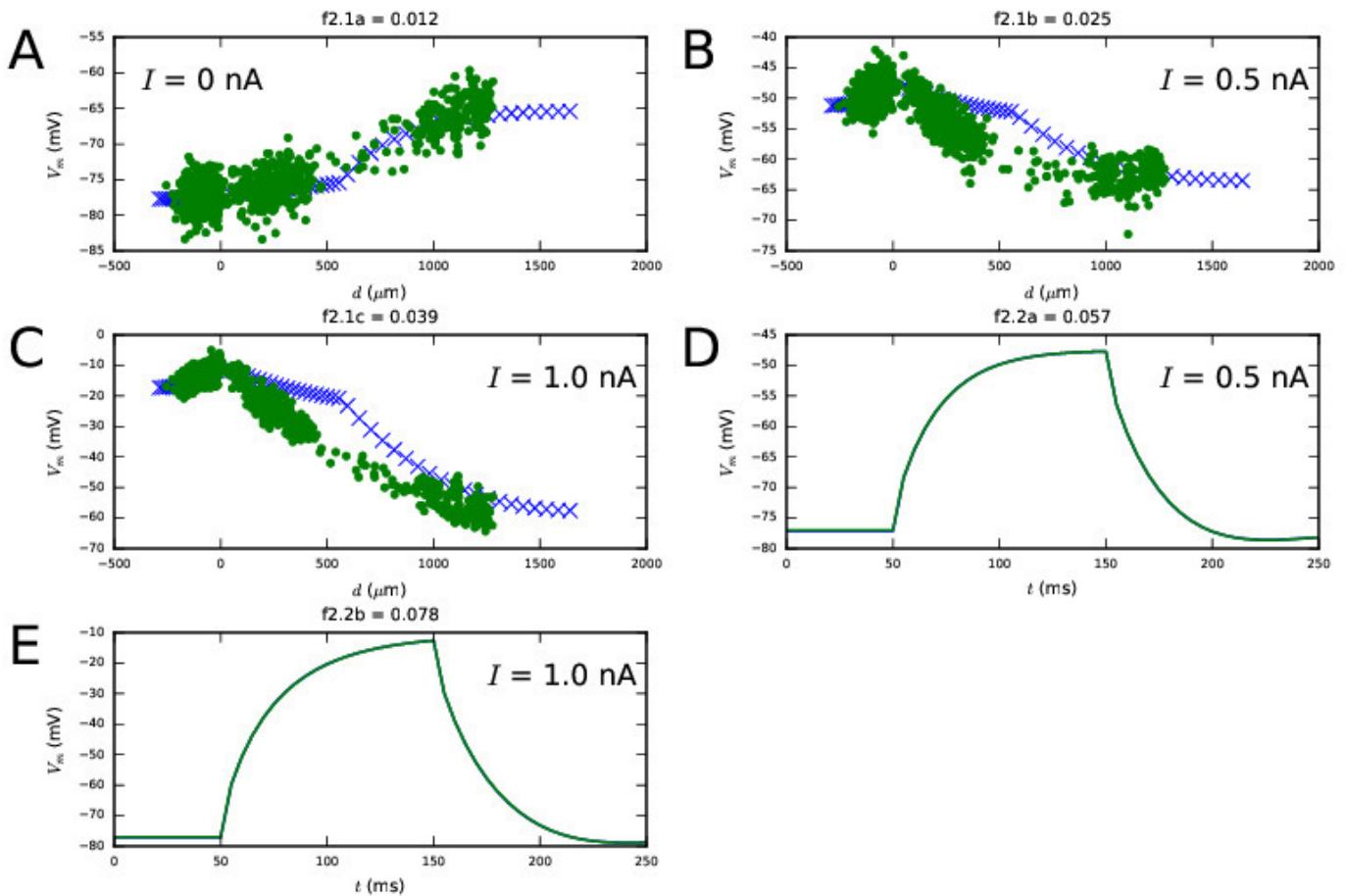

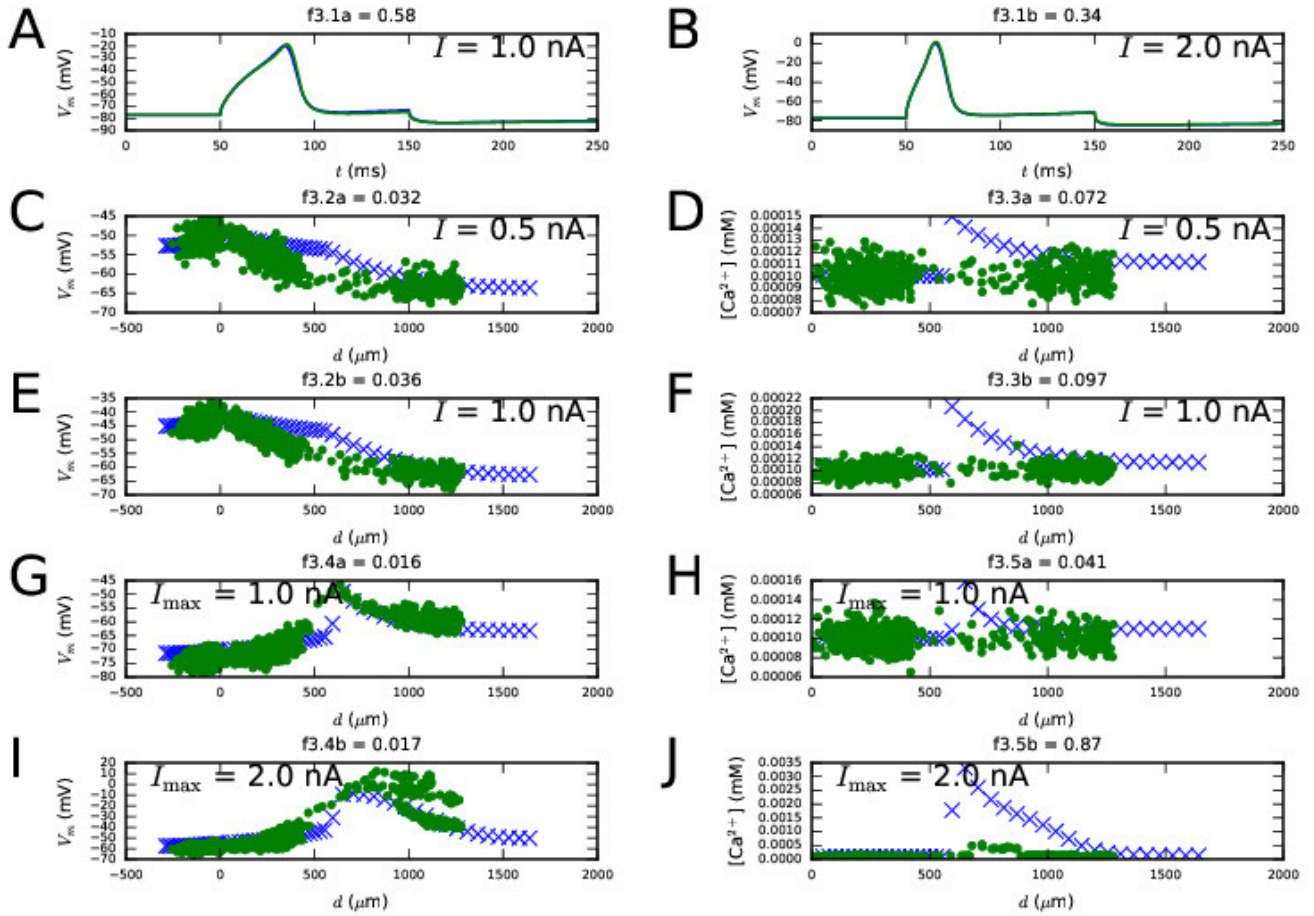Figure S8: **Second step fit using noisy dendritic measurements**. See Figure 2.

Figure S9: **Third step fit using noisy dendritic measurements**. See Figure 3.

Table S6: **Parameter values obtained from the multi-objective optimizations of Figures S7–S10**. See Table 3 for the corresponding parameter values obtained from fitting to noiseless data.

| STEP 1		STEP 2		STEP 3		STEP 4	
Variable	Value	Variable	Value	Variable	Value	Variable	Value
L^{soma}	41.2	E_h	-39.7	$g_{\text{CaHVA}}^{\text{soma}}$	0.000826	$g_{\text{Nat}}^{\text{soma}}$	3.71
L^{basal}	501	g_h^{soma}	0.000177	$g_{\text{CaLVA}}^{\text{soma}}$	0.00588	$g_{\text{Nap}}^{\text{soma}}$	0
L^{apic}	$1.3\cdot10^3$	g_h^{basal}	0.000244	γ^{soma}	0.000637	$g_{\text{Kt}}^{\text{soma}}$	0.1
L^{tuft}	742	g_h^{apic}	0.00203	$\tau\text{decay}^{\text{soma}}$	400	$g_{\text{Kp}}^{\text{soma}}$	0
R_a^{soma}	229	g_h^{tuft}	0.0146	$g_{\text{SK}}^{\text{soma}}$	0.0328	$g_{Kv3.1}^{\text{soma}}$	0.549
R_a^{basal}	122	g_l^{soma}	$2.97\cdot10^{-5}$	$g_{\text{CaHVA}}^{\text{apic}}$	$1.53\cdot10^{-7}$	g_m^{apic}	0.000172
R_a^{apic}	190	g_l^{basal}	$7.18\cdot10^{-5}$	$g_{\text{CaLVA}}^{\text{apic}}$	0.0224	$g_{\text{Nat}}^{\text{apic}}$	0.0196
R_a^{tuft}	984	g_l^{apic}	0.0001	γ^{apic}	0.0005	$g_{Kv3.1}^{\text{apic}}$	0.00228
c_m^{soma}	0.688	g_l^{tuft}	0.0001	$\tau\text{decay}^{\text{apic}}$	43	g_m^{apic}	$7.71\cdot10^{-5}$
c_m^{basal}	3.27			$g_{\text{SK}}^{\text{apic}}$	0.00231	$g_{\text{Nat}}^{\text{tuft}}$	0.00472
c_m^{apic}	3.26			$g_{\text{CaHVA}}^{\text{tuft}}$	0.0152	$g_{Kv3.1}^{\text{tuft}}$	0.0132
c_m^{tuft}	2.61			$g_{\text{CaLVA}}^{\text{tuft}}$	0.248		
g_l^{soma}	$3.02\cdot10^{-5}$			γ^{tuft}	0.0232		
g_l^{basal}	$7.02\cdot10^{-5}$			$\tau\text{decay}^{\text{tuft}}$	151		
g_l^{apic}	$9.73\cdot10^{-5}$			$g_{\text{SK}}^{\text{tuft}}$	0.00392		
g_l^{tuft}	$9.27\cdot10^{-5}$						
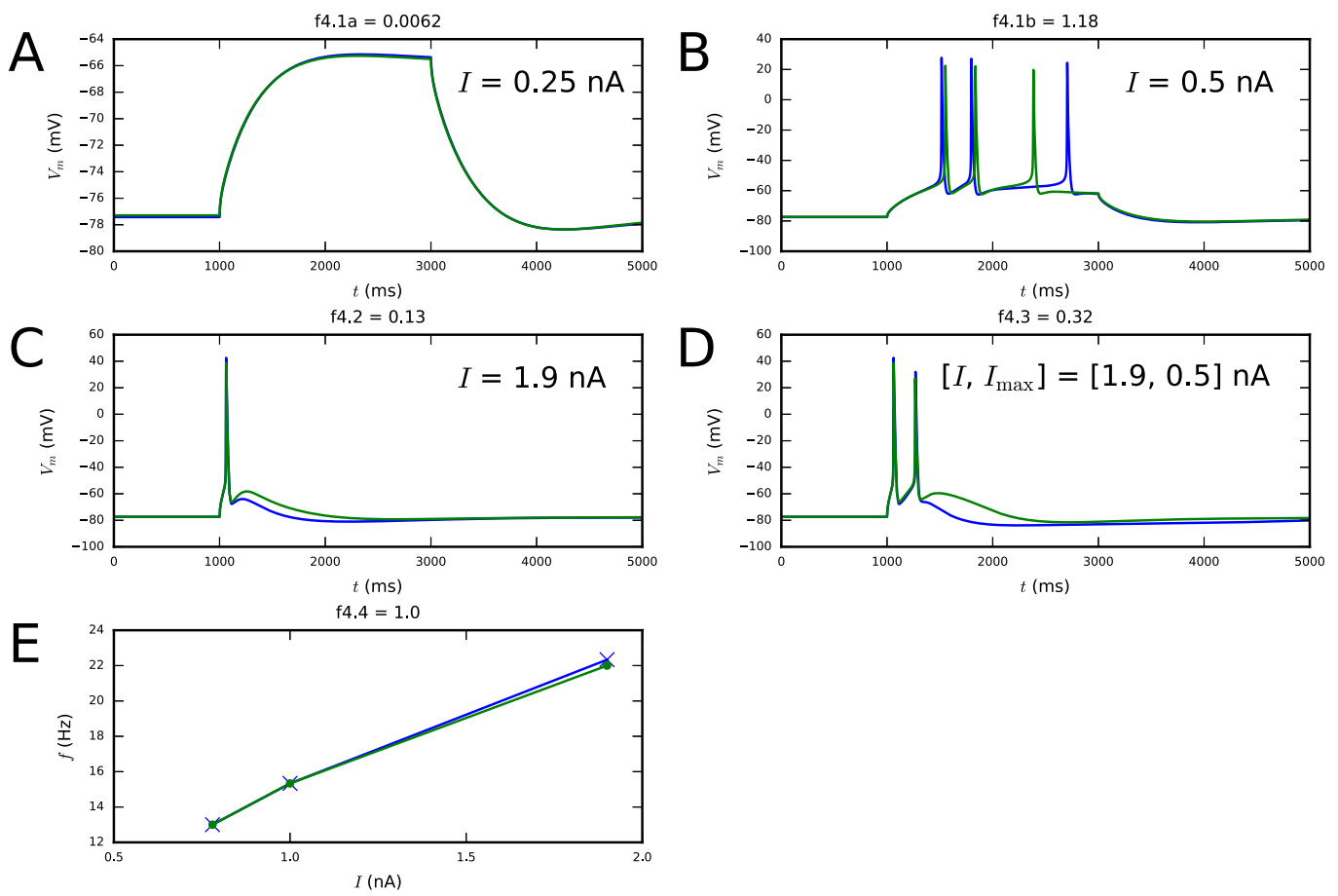
Figure S10: **Fourth step fit using parameters from previous step fits with noisy dendritic measurements.** See Figure 4.

S6 Fitting stepwise to temporally downsampled target data

Here, we downsampled the membrane potential measurements at the dendrites using 100-Hz sampling frequency, and the Ca^{2+} concentration measurements at the dendrites using 10-Hz sampling frequency. We compared the results of the second step optimization using the downsampled target data with those obtained using accurate data. Figure S11 shows the objective function values $f_{2.1}$ and $f_{2.2}$ of a population of $N = 4000$ particles after 60 evolutionary algorithm iterations from ten independent trials. Figures S12 and S13, by contrast, show the distribution of function $f_{2.1}$ and $f_{2.2}$ values, respectively, against the underlying parameter values. In all three figures, the distributions corresponding to accurate target data were indistinguishable from those corresponding to lower resolution target data. We confirmed this using U-test, which gave values larger than 0.05 for all parameter and objective function value distributions.
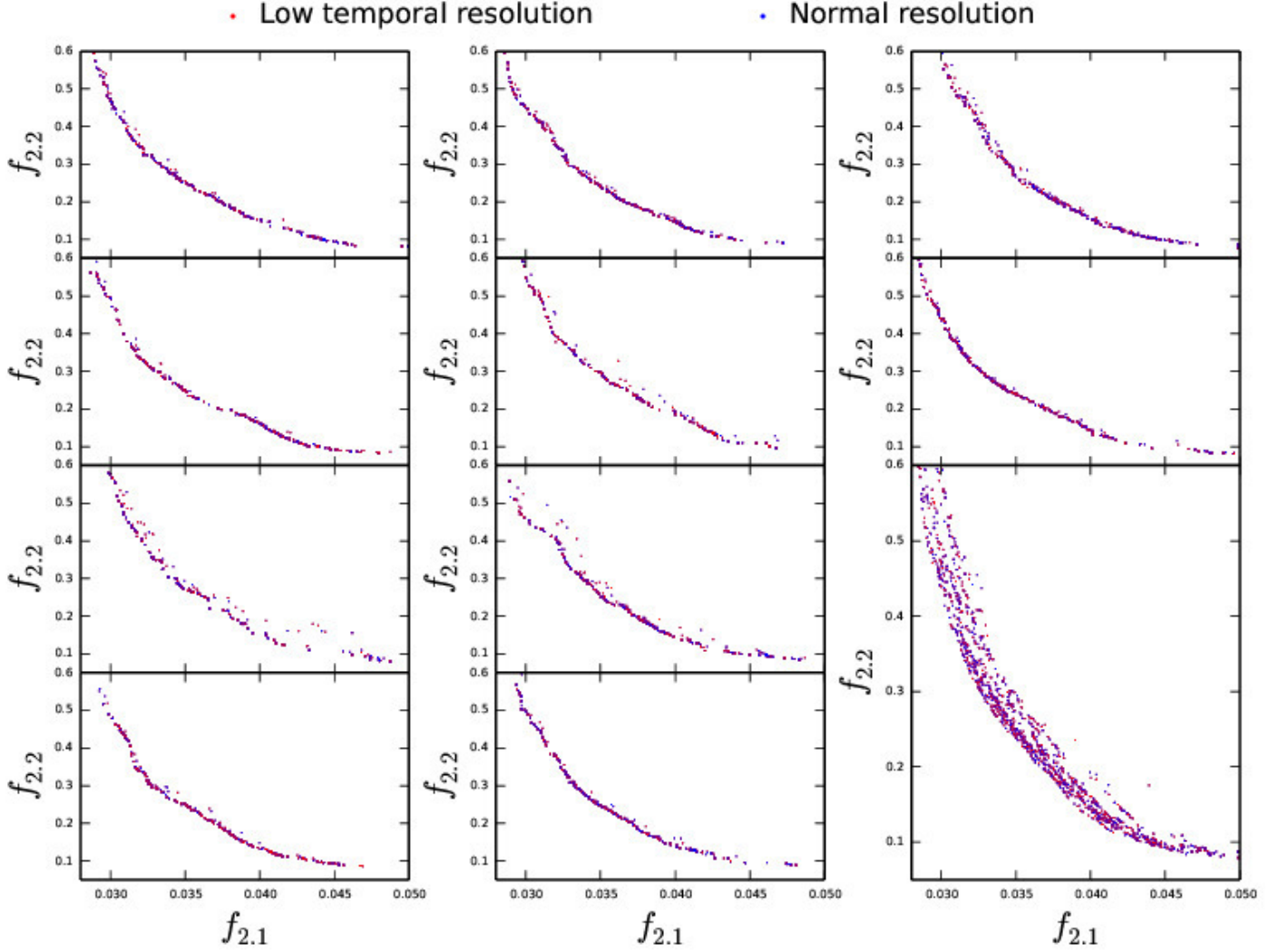

Figure S11: **Objective function values in the second step optimization — differences between fitting to accurate and temporally downsampled target data**. The ten small panels show ten repetitions of the same optimization procedure (each with different random number seed). The axes show the objective function values $f_{2.1}$ and $f_{2.2}$ for the $N = 4000$ particles after 60 generations. Red: optimization with target data, where the dendritic membrane-potential measurements are acquired with a 100-Hz sampling frequency and the dendritic Ca^{2+} concentration measurements with a 10-Hz sampling frequency. Blue: optimization with accurate target data. The large panel shows the combined data.
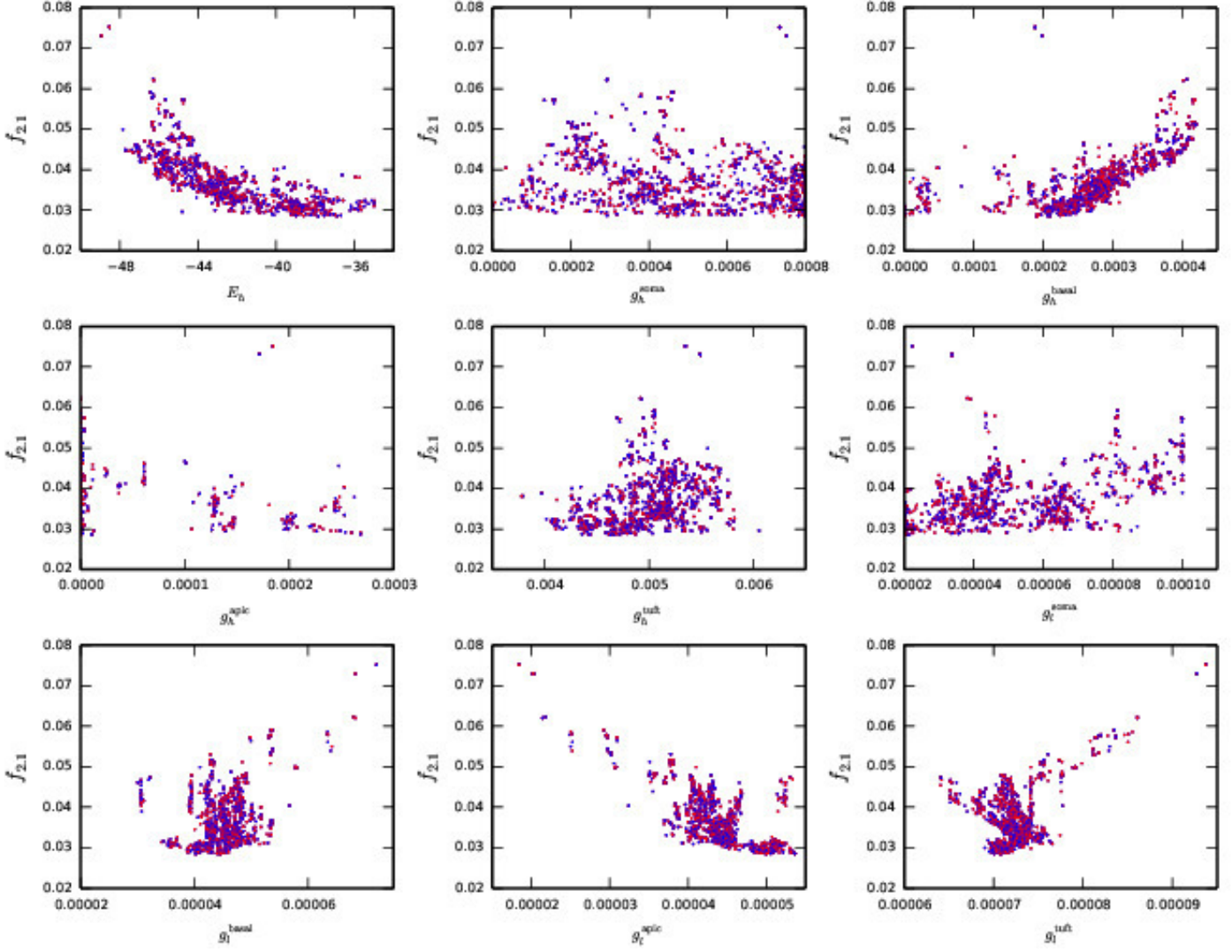
Figure S12: **Parameter values in the second step optimization plotted against the values of $f_{2.1}$ — differences between fitting to accurate and temporally downsampled target data**. The different panels show values of different model parameters fitted during the second step. Combined data from ten independent trials (see Figure S11). Red: optimization with target data, where the dendritic membrane-potential measurements are acquired with a 100-Hz sampling frequency and the dendritic Ca^{2+} concentration measurements with a 10-Hz sampling frequency. Blue: optimization with accurate target data. The reversal potential parameter values are given in mV and the conductance parameter values in S/cm^2.
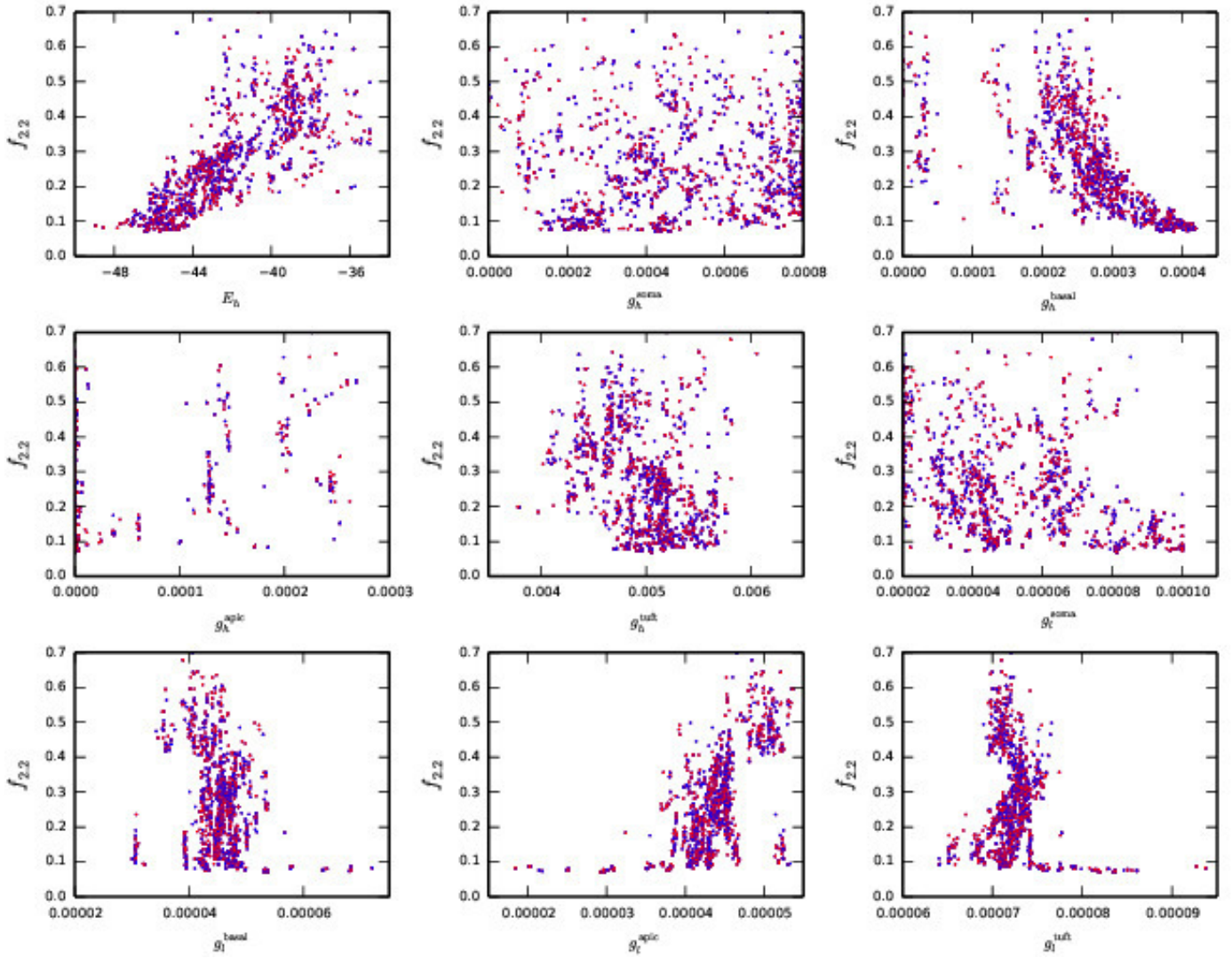
13

Figure S13: **Parameter values in the second step optimization plotted against the values of $f_{2.2}$ — differences between fitting to accurate and temporally downsampled target data**. The different panels show values of different model parameters fitted during the second step. Combined data from ten independent trials (see Figure S11). Red: optimization with target data, where the dendritic membrane-potential measurements are acquired with a 100-Hz sampling frequency and the dendritic Ca^{2+} concentration measurements with a 10-Hz sampling frequency. Blue: optimization with accurate target data. The reversal potential parameter values are given in mV and the conductance parameter values in S/cm^2.

S7 Fitting with predetermined leak conductance

If the purpose of the fitting is to reduce a neuron model with complex morphology with a reduced-morphology model (as in our case), an alternative procedure can be chosen for the first step. Here, following the procedure of [S5], we set the leak conductances to a set value, 5×10^{-5} S/cm^2, in both the reduced (fitted) model and the model with full morphology (data). The rest of the parameters of the first step (section lengths, membrane capacitances, and axial resistances) were fitted normally, and likewise the parameters of the second to fourth steps were fitted according to Tables 1 and 2. Figures S14–S17 illustrate the fitting results of the four steps using this scheme, and show that an acceptable fit was obtained also using this procedure.
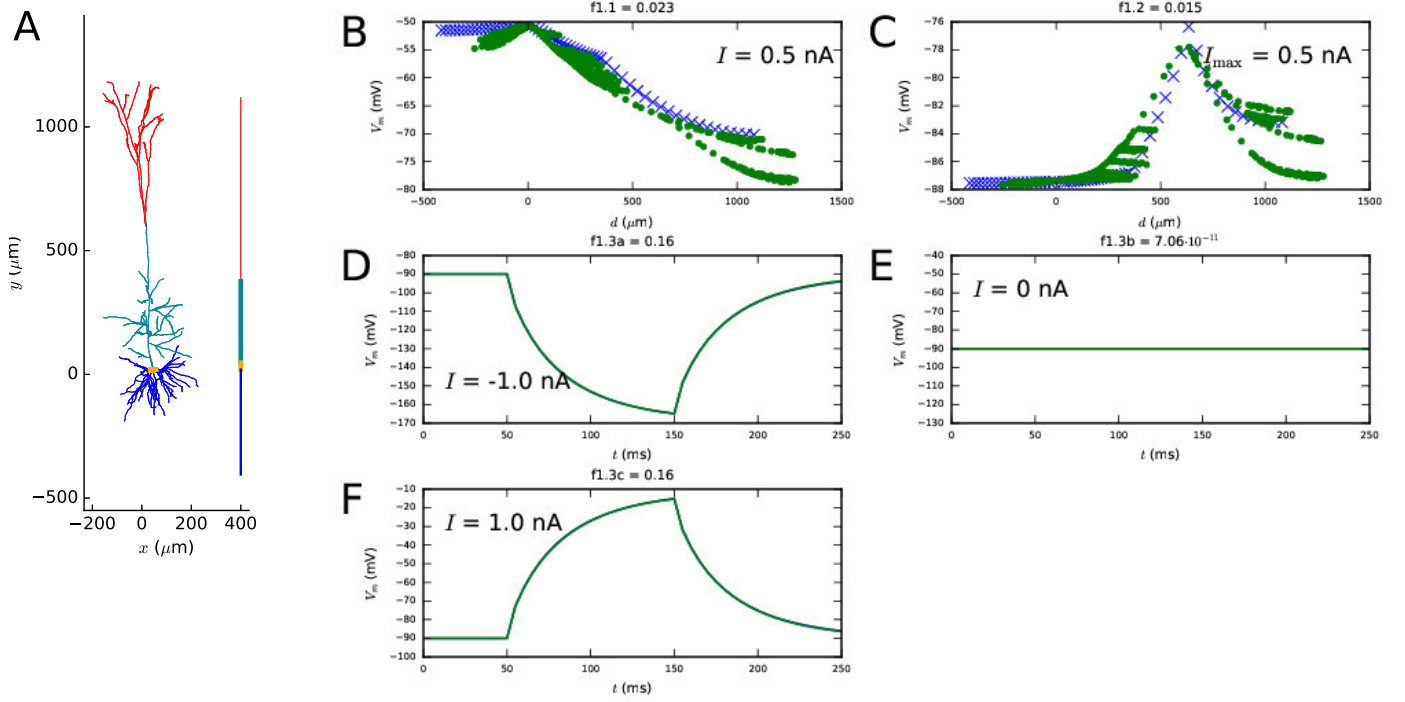

Figure S14: **First step fit using the scheme where the leak conductance is explicitly set to a fixed value both in the data and in the fitted model during the first step**. See Figure 1 for the corresponding figure for fitting of parameters according to Table 1.

Table S7: **Parameter values obtained from the multi-objective optimizations of Figures S14–S17**. See Table 3 for the corresponding parameter values obtained from the optimizations where passive conductances are fitted during both first and second step.

| STEP 1		STEP 2		STEP 3		STEP 4	
Variable	Value	Variable	Value	Variable	Value	Variable	Value
L^{soma}	28	E_h	-40.6	$g_{\text{CaHVA}}^{\text{soma}}$	0.000669	$g_{\text{Nat}}^{\text{soma}}$	2.25
L^{basal}	424	g_h^{soma}	0.000107	$g_{\text{CaLVA}}^{\text{soma}}$	0.00943	$g_{\text{Nap}}^{\text{soma}}$	0.00449
L^{apic}	329	g_h^{basal}	0.000194	γ^{soma}	0.0005	$g_{\text{Kt}}^{\text{soma}}$	0.0294
L^{tuft}	743	g_h^{apic}	$8.89 \cdot 10^{-5}$	$\tau \text{decay}^{\text{soma}}$	597	$g_{\text{Kp}}^{\text{soma}}$	0
R_a^{soma}	442	g_h^{tuft}	0.00457	$g_{\text{SK}}^{\text{soma}}$	0.0555	$g_{Kv3.1}^{\text{soma}}$	1.16
R_a^{basal}	230	g_l^{soma}	$6.05 \cdot 10^{-5}$	$g_{\text{CaHVA}}^{\text{apic}}$	$6.8 \cdot 10^{-5}$	g_m^{apic}	$6.26 \cdot 10^{-5}$
R_a^{apic}	933	g_l^{basal}	$2.17 \cdot 10^{-5}$	$g_{\text{CaLVA}}^{\text{apic}}$	$5.04 \cdot 10^{-6}$	$g_{\text{Nat}}^{\text{apic}}$	0.0182
R_a^{tuft}	292	g_l^{apic}	$5.88 \cdot 10^{-5}$	γ^{apic}	0.0471	$g_{Kv3.1}^{\text{apic}}$	0.00218
c_m^{soma}	1.36	g_l^{tuft}	$6.34 \cdot 10^{-5}$	$\tau \text{decay}^{\text{apic}}$	135	g_m^{apic}	$8.15 \cdot 10^{-5}$
c_m^{basal}	1.78			$g_{\text{SK}}^{\text{apic}}$	0	$g_{\text{Nat}}^{\text{tuft}}$	0.0129
c_m^{apic}	1.17			$g_{\text{CaHVA}}^{\text{tuft}}$	0	$g_{Kv3.1}^{\text{tuft}}$	0.0023
c_m^{tuft}	3.15			$g_{\text{CaLVA}}^{\text{tuft}}$	0.0262		
				γ^{tuft}	0.000942		
				$\tau \text{decay}^{\text{tuft}}$	109		
				$g_{\text{SK}}^{\text{tuft}}$	0.0013		
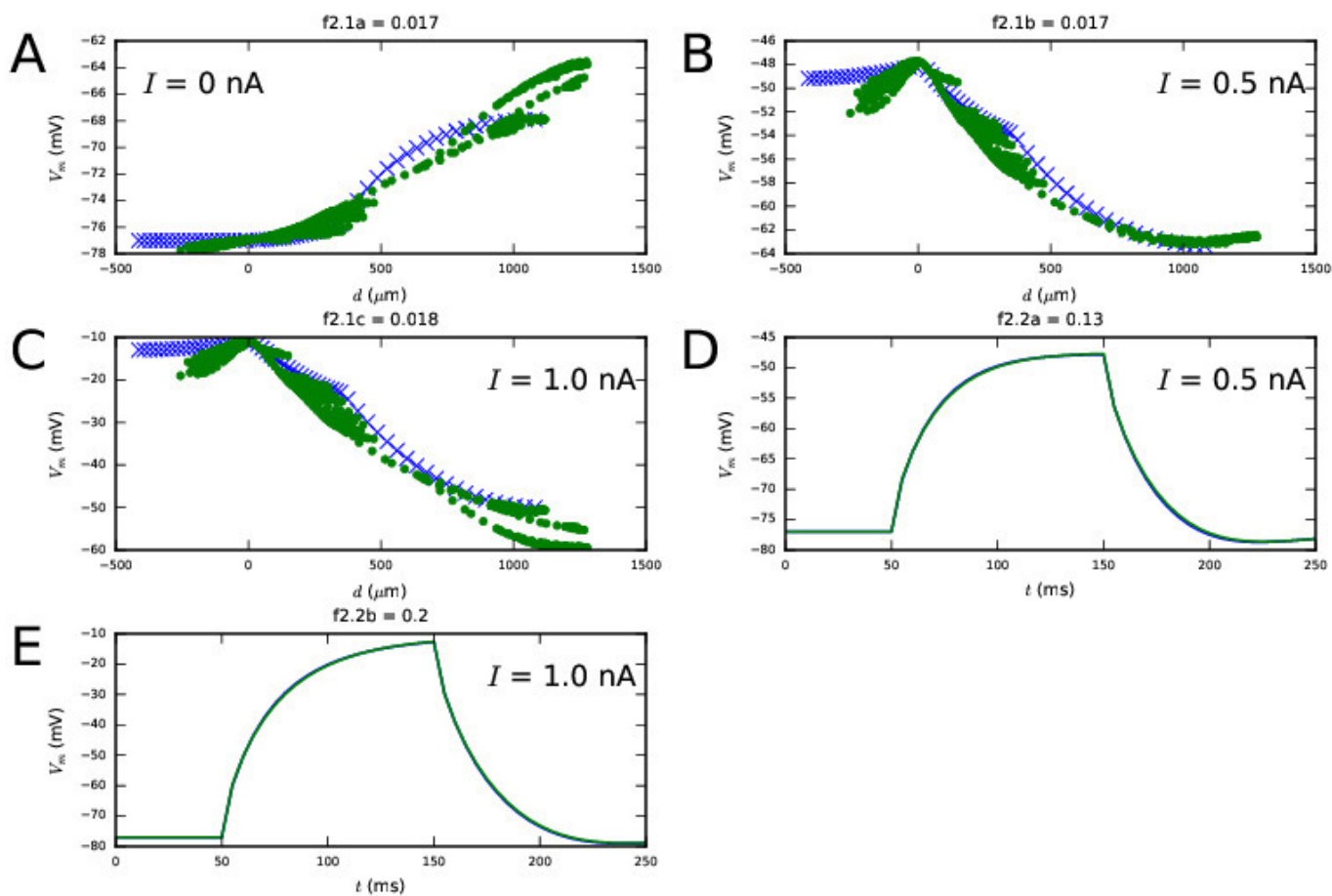
Figure S15: **Second step fit using the scheme with fixed leak channel conductances during the first step.** See Figure 2.
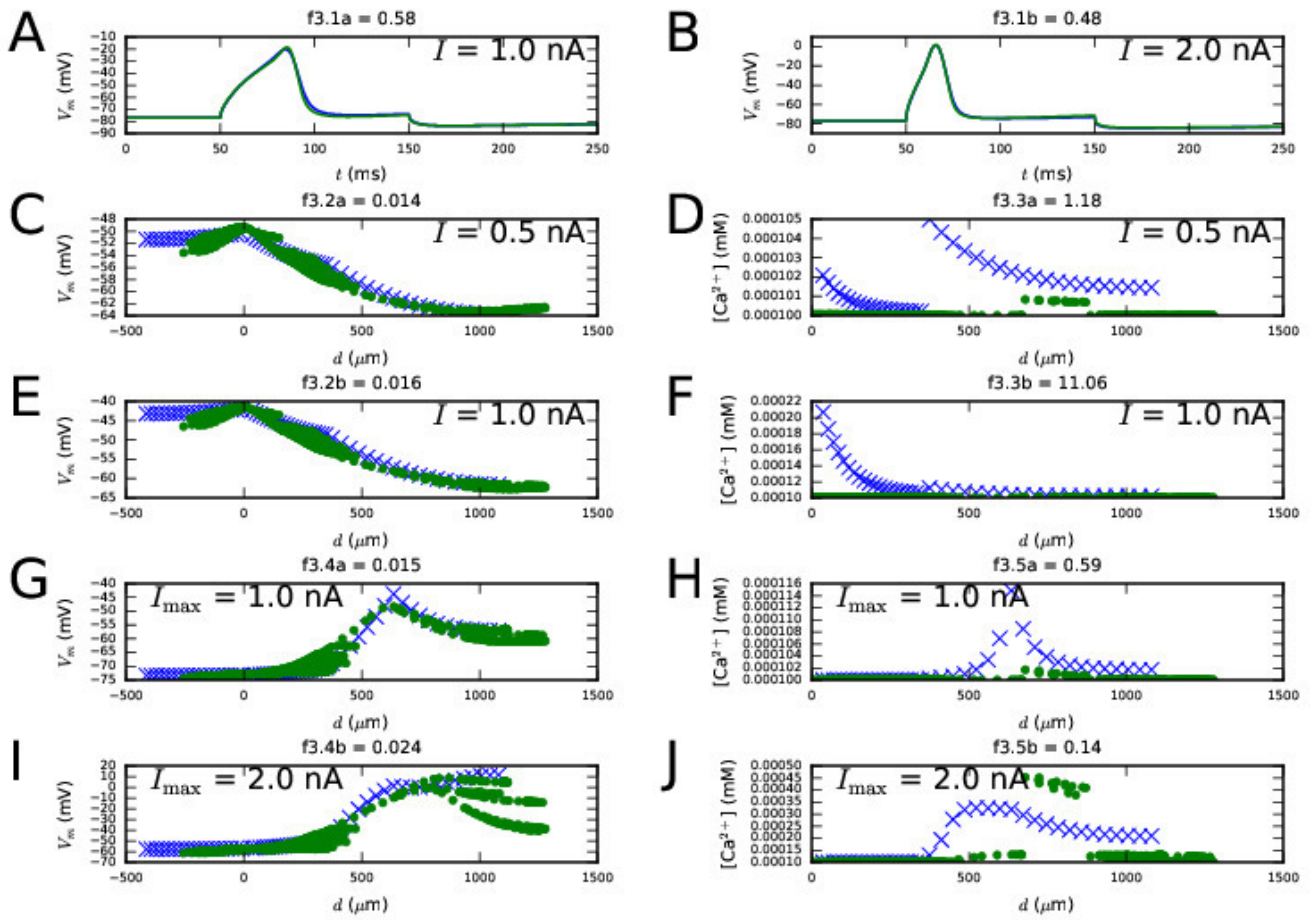
Figure S16: **Third step fit using the scheme with fixed leak channel conductances during the first step**. See Figure 3.
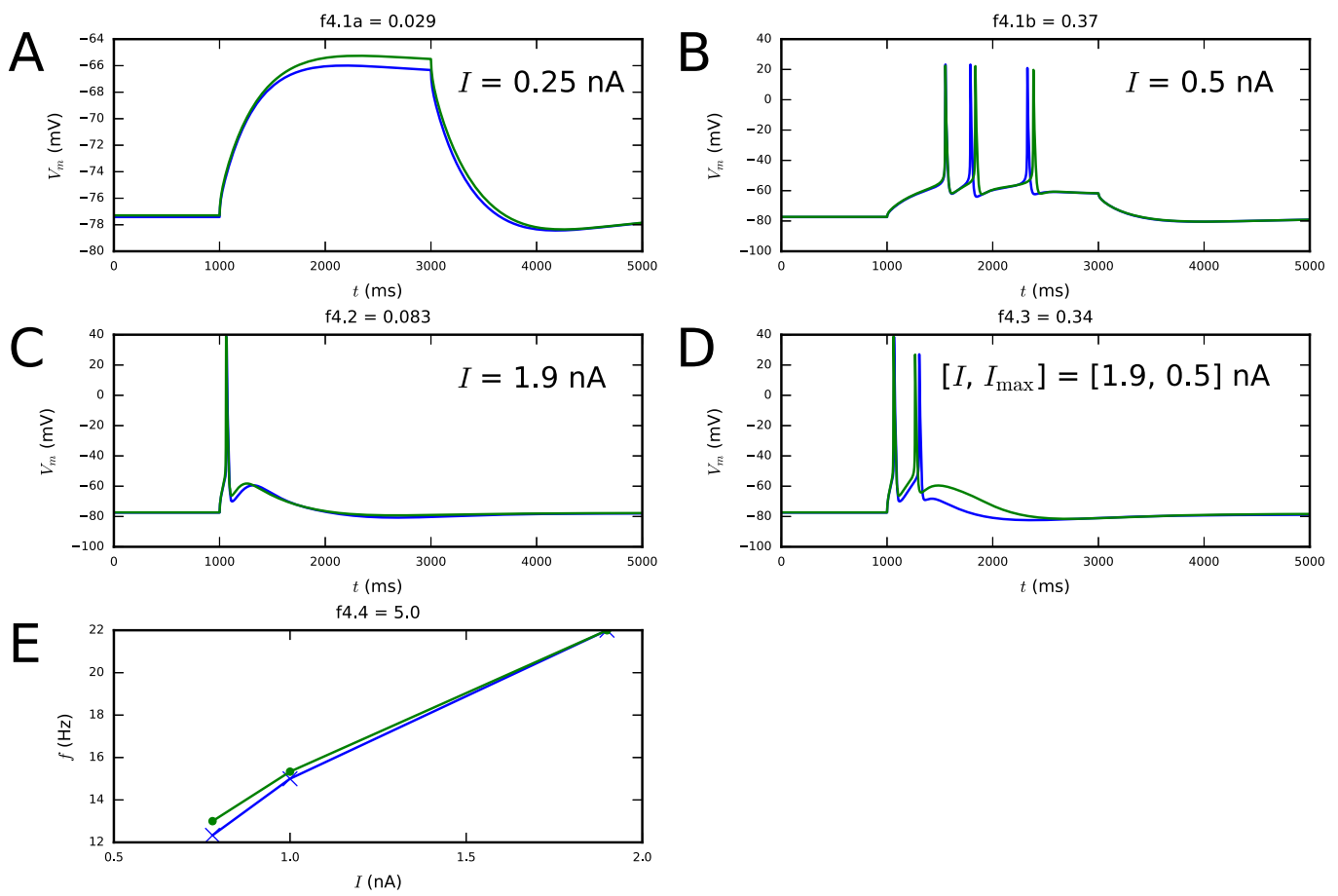
Figure S17: **Fourth step fit using the scheme with fixed leak channel conductances during the first step.** See Figure 4.

S8 Fitting stepwise by passing the whole population of solutions to the next step

Instead of choosing at the end of each step the best candidate parameter set (see Section 2.2.6) and passing it to the next step fitting, the whole population can be passed on to the next step. In this section, we applied this approach. Each particle in the further steps had both variables that were being fitted (see Table 1) and variables that had been fitted during the previous steps. We modified the genetic algorithm such that only the variables that were fitted were applied to the NSGA crossover mechanism, while the variables of the earlier steps were chosen in an all-or-none fashion such that one of the parent particles (randomly chosen) was made the dominant particle, and all previous-step variable values were taken from that particle. Figures S18–S21 illustrate the fitting results of the four steps using this scheme, and show that an acceptable (albeit slightly worse for the early steps) fit was obtained also using this procedure.
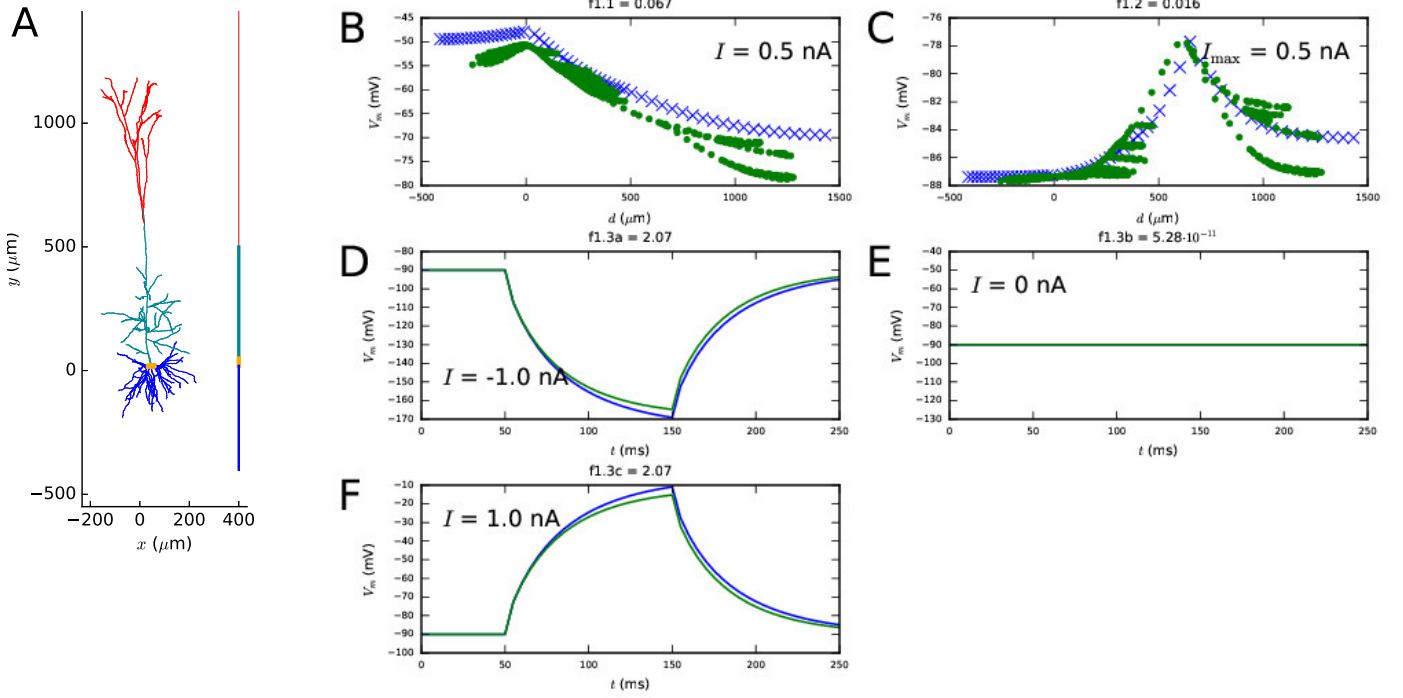

Figure S18: **First step fit using the scheme where the whole population of parameter sets is passed on to the next step**. See Figure 1 for the corresponding figure of the scheme of Section 2.2.6.

Table S8: **Parameter values obtained from the multi-objective optimizations of Figures S18–S21**. See Table 3 for the corresponding parameter values obtained from the standard scheme as described in Section 2.2.6.

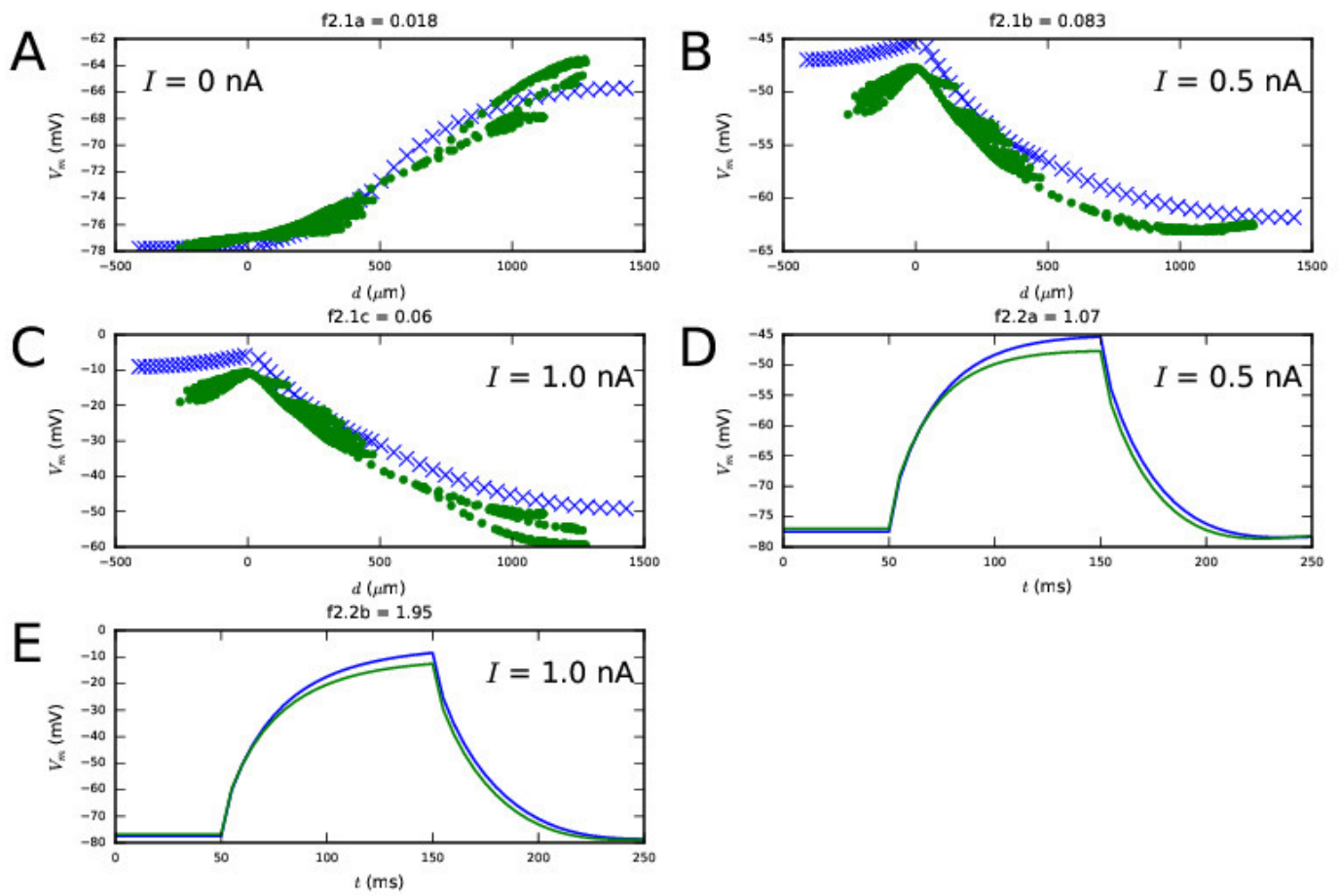| STEP 1		STEP 2		STEP 3		STEP 4	
Variable	Value	Variable	Value	Variable	Value	Variable	Value
L^{soma}	29.8	E_h	-48.9	$g_{\text{CaHVA}}^{\text{soma}}$	0.000837	$g_{\text{Nat}}^{\text{soma}}$	2.24
L^{basal}	420	g_h^{soma}	0.000678	$g_{\text{CaLVA}}^{\text{soma}}$	0.000896	$g_{\text{Nap}}^{\text{soma}}$	0.000295
L^{apic}	451	g_h^{basal}	0.000184	γ^{soma}	0.0005	$g_{\text{Kt}}^{\text{soma}}$	0.0515
L^{tuft}	976	g_h^{apic}	0	$\tau\text{decay}^{\text{soma}}$	527	$g_{\text{Kp}}^{\text{soma}}$	0
R_a^{soma}	460	g_h^{tuft}	0.0094	$g_{\text{SK}}^{\text{soma}}$	0.0506	$g_{Kv3.1}^{\text{soma}}$	0.616
R_a^{basal}	172	g_l^{soma}	$3.16\cdot10^{-5}$	$g_{\text{CaHVA}}^{\text{apic}}$	0	g_m^{apic}	0.0005
R_a^{apic}	925	g_l^{basal}	$4.42\cdot10^{-5}$	$g_{\text{CaLVA}}^{\text{apic}}$	0.00678	$g_{\text{Nat}}^{\text{apic}}$	0.00863
R_a^{tuft}	104	g_l^{apic}	$4.87\cdot10^{-5}$	γ^{apic}	0.00365	$g_{Kv3.1}^{\text{apic}}$	0.0119
c_m^{soma}	1.26	g_l^{tuft}	$5.36\cdot10^{-5}$	$\tau\text{decay}^{\text{apic}}$	58	g_m^{apic}	0.000188
c_m^{basal}	2.35			$g_{\text{SK}}^{\text{apic}}$	0	$g_{\text{Nat}}^{\text{tuft}}$	0.00819
c_m^{apic}	1.29			$g_{\text{CaHVA}}^{\text{tuft}}$	0.0111	$g_{Kv3.1}^{\text{tuft}}$	0.0109
c_m^{tuft}	2.65			$g_{\text{CaLVA}}^{\text{tuft}}$	0.0185		
				γ^{tuft}	0.043		
				$\tau\text{decay}^{\text{tuft}}$	21		
				$g_{\text{SK}}^{\text{tuft}}$	0.00418		

Figure S19: **Second step fit using the scheme where the whole population of parameter sets is passed on to the next step**. See Figure 2.
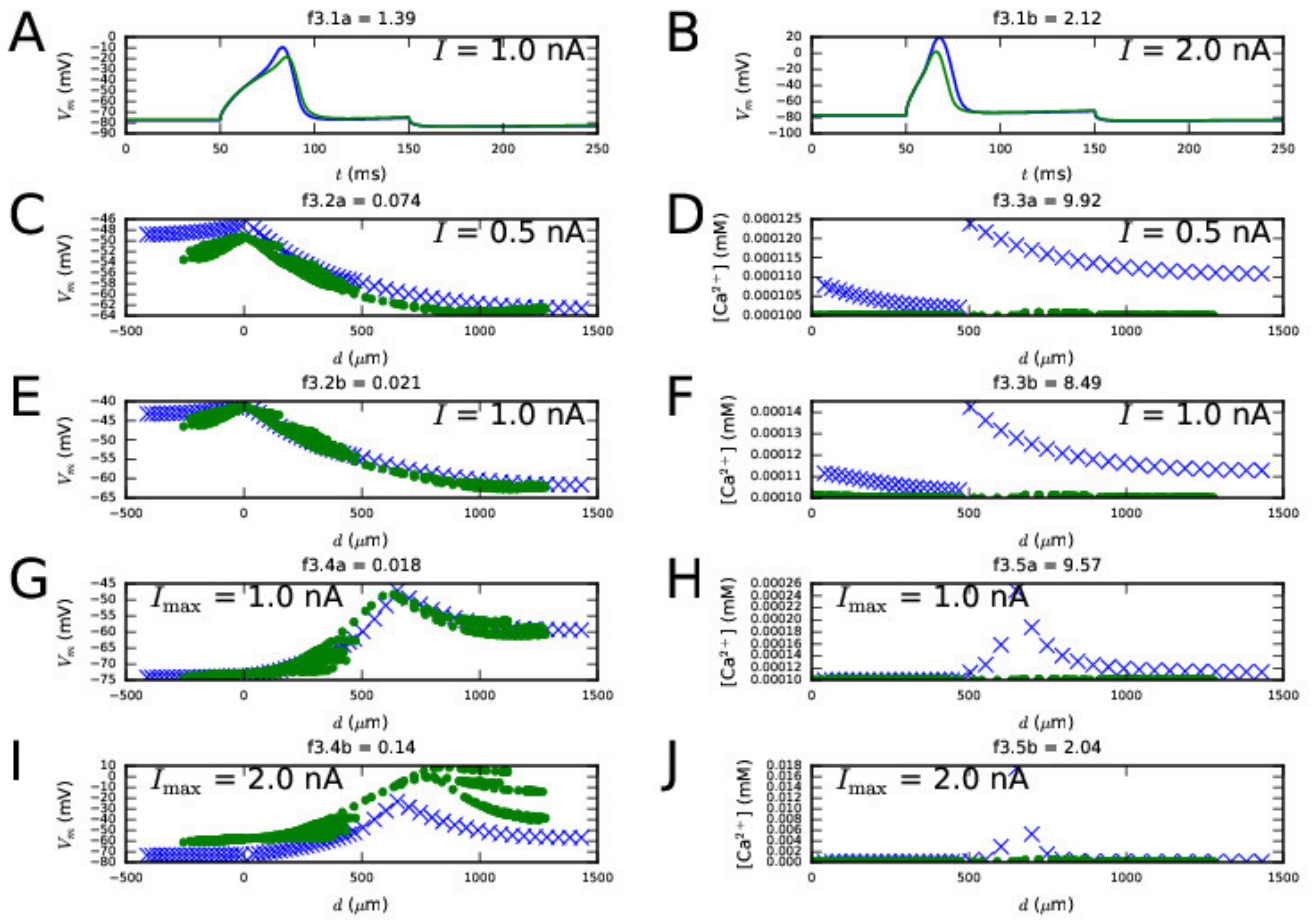
Figure S20: **Third step fit using the scheme where the whole population of parameter sets is passed on to the next step**. See Figure 3.
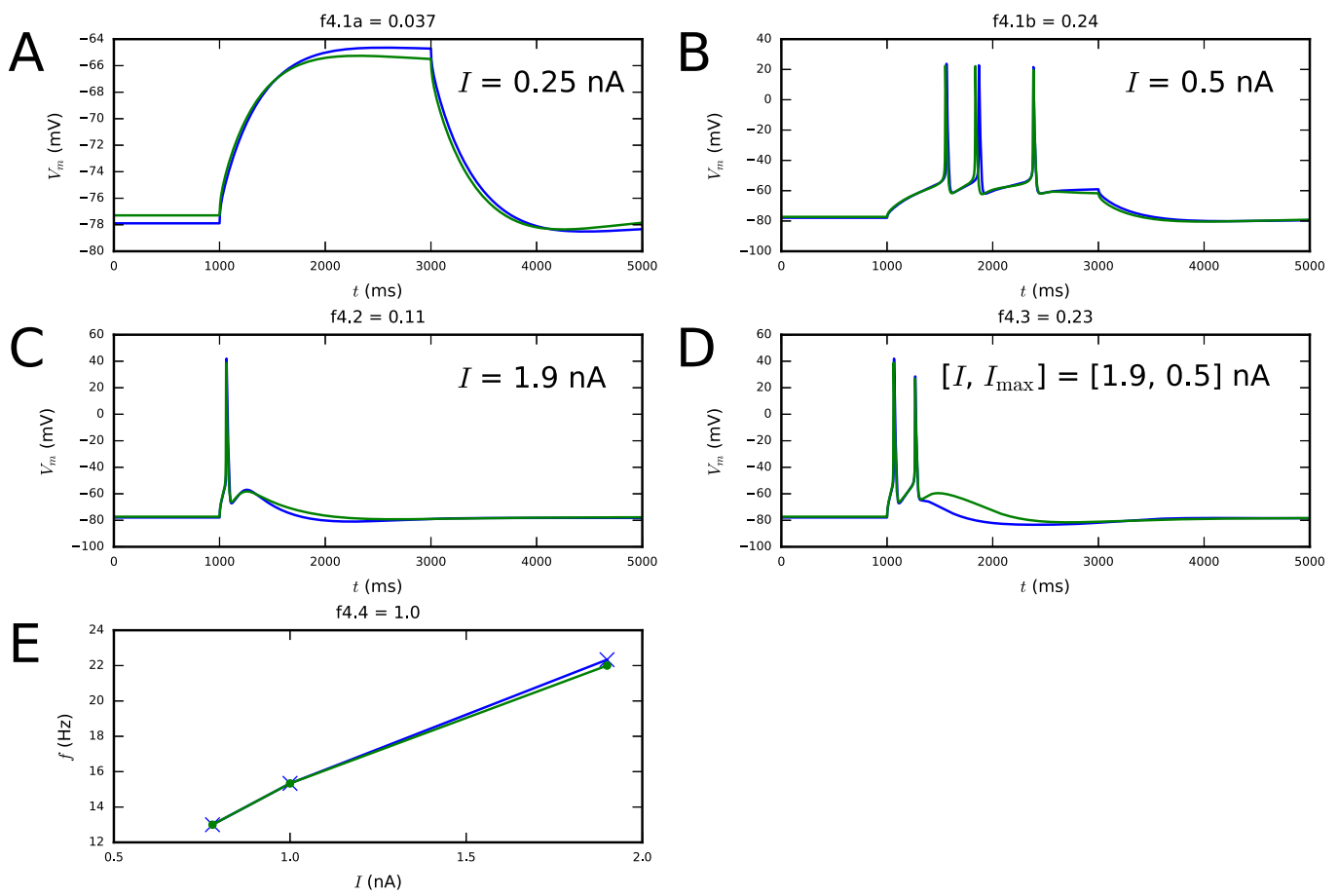
Figure S21: **Fourth step fit using the scheme where the whole population of parameter sets is passed on to the next step**. See Figure 4.

S9 Fitting a neuron model with reconstructed morphology

In this section, we applied our method to fit the conductance parameters along a reconstructed morphology. We used the cell #2 of [S1] as the morphology for the fitted model (in contrast to the target data which was generated using cell #1), and divided the dendro-somatic segments of this morphology to five groups: basal dendrite, soma, proximal apical dendrite, apical trunk, and apical tuft. In addition, the axonal segments were kept as a separate group, where only passive parameters (axial resistance, capacitance, and leak conductance) were fitted. The separation between apical groups was made such that the segments in the apical dendrite whose mid-point was up to 500 μm from the soma belonged to the proximal apical dendrite, while the segments whose mid-point was between 500 and 800 μm belonged to the apical trunk, and segments further than 800 μm belonged to the apical tuft. All segments in the same group had identical model parameters (conductances, capacitance and axial resistance).

As there was no need for fitting morphological parameters, we combined the first two steps in our four-step scheme, while we kept the last two steps unchanged. The adapted objective functions are given in Table S9. Figures S22–S24 show that our method succeeded in fitting the model parameters of a neuron model with a complex morphology as well, and the obtained parameter values are given in Table S10. Future studies should, however, optimize the way the conductances are parametrized in order to better reproduce the observed shapes of ion-channel distributions [S6], [S7]. Ultimately, if there exist target data containing measurements along different dendritic branches, the fitting methods should be designed to fit the conductance parameters along the reconstructed morphology to these data in order to better represent the dendritic computations that take place in the neuron.

Table S9: **Objective functions used when fitting a neuron model with reconstructed morphology**. The first column shows the objective number, and the corresponding objective number in the default four-step method is given in parenthesis. The rest of the columns are shown in the same way as in Table 2.

| Objective number	Objective function	Where measured	Stimulus type	Eq.	Stimulus amplitude
1.1(1.1 & 2.1)	Difference in distribution of steady-state membrane potential	Dendrites	3000-ms DC pulse at soma	(5)	0.0 nA 0.5 nA 1.0 nA
1.2(1.2)	Difference in distribution of peak membrane potential	Dendrites	EPSP-like current injection at the apical dendrite 620 μm from soma	(5)	0.5 nA 1.0 nA
1.3(1.3 & 2.2)	Difference in membrane potential time series	Soma	100-ms DC pulse at soma	(2)	0.5 nA 1.0 nA
2.1(3.1)	Difference in membrane potential time series	Soma	100ms DC pulse at soma	(2)	1.0 nA 2.0 nA
2.2(3.2)	Difference in distribution of steady-state membrane potentials	Dendrites	3000-ms DC pulse at soma	(5)	0.5 nA 1.0 nA
2.3(3.3)	Difference in distribution of steady-state intracellular $[Ca^{2+}]$	Apical dendrite	3000-ms DC pulse at soma	(5)	0.5 nA 1.0 nA
2.4(3.4)	Difference in distribution of peak membrane potential	Dendrites	EPSP-like current injection at the apical dendrite 620 μm from soma	(5)	0.5 nA 1.0 nA
2.5(3.5)	Difference in distribution of peak intracellular $[Ca^{2+}]$	Apical dendrite	EPSP-like current injection at the apical dendrite 620 μm from soma	(5)	0.5 nA 1.0 nA
3.1(4.1)	Difference in membrane potential time series and numbers of spikes	Soma	100-ms DC pulse at soma	(4)	0.25 nA 0.5 nA
3.2(4.2)	Difference in membrane potential time series and numbers of spikes	Soma	5-ms DC at soma	(4)	1.9 nA
3.3(4.3)	Difference in membrane potential time series and numbers of spikes	Soma	5-ms DC at soma and EPSP-like current at apical dendrite	(4)	1.9 nA (soma) + 0.5 nA (apical)
3.4(4.4)	Difference in numbers of spikes	Soma	3000-ms DC at soma	(3)	0.78 nA 1.0 nA 1.9 nA
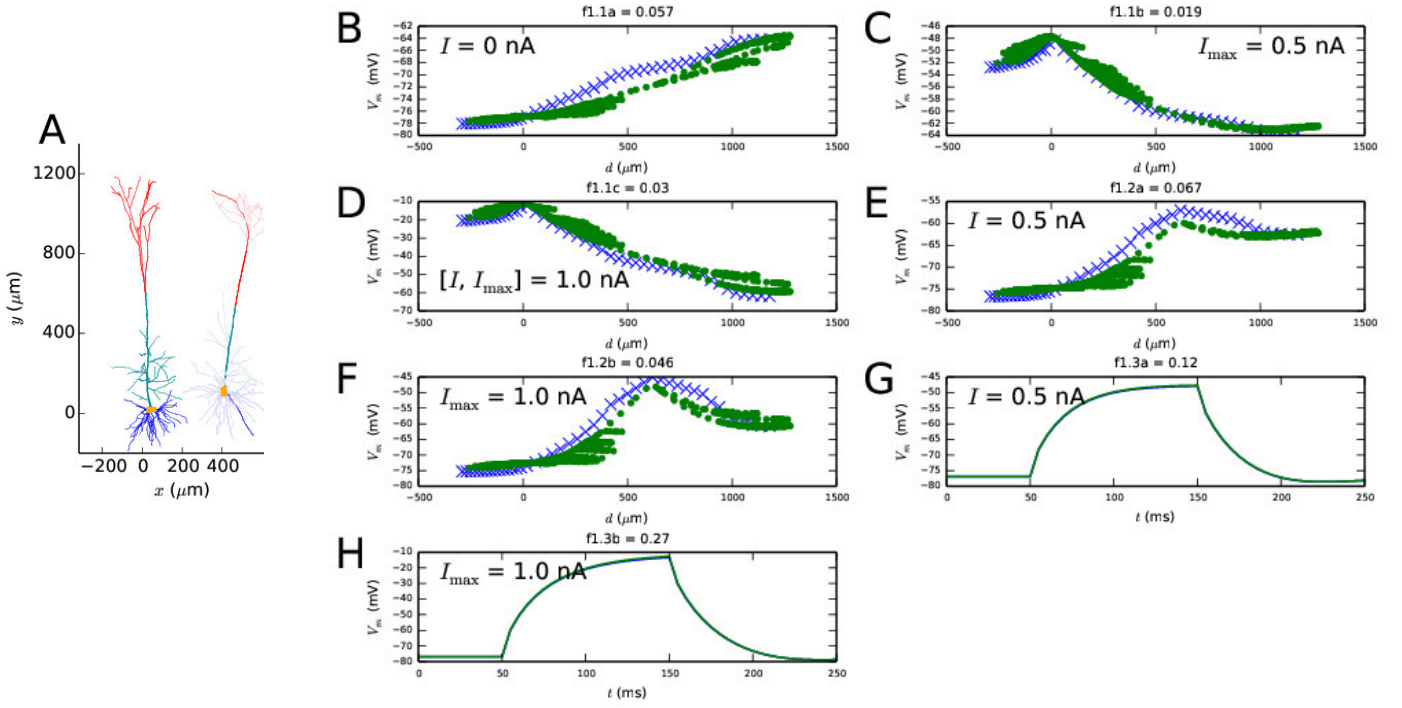
Figure S22: **First step in the fitting of the model with reconstructed morphology**. In the morphology of the fitted model in panel A, the dendritic branches along which the membrane potentials and Ca^{2+} concentrations were recorded are highlighted, while other dendritic branches are plotted with dim colors. See Table S9 for the corresponding objective functions and Figures 1 and 2 for the corresponding plots in the default four-step scheme for reduced morphology.
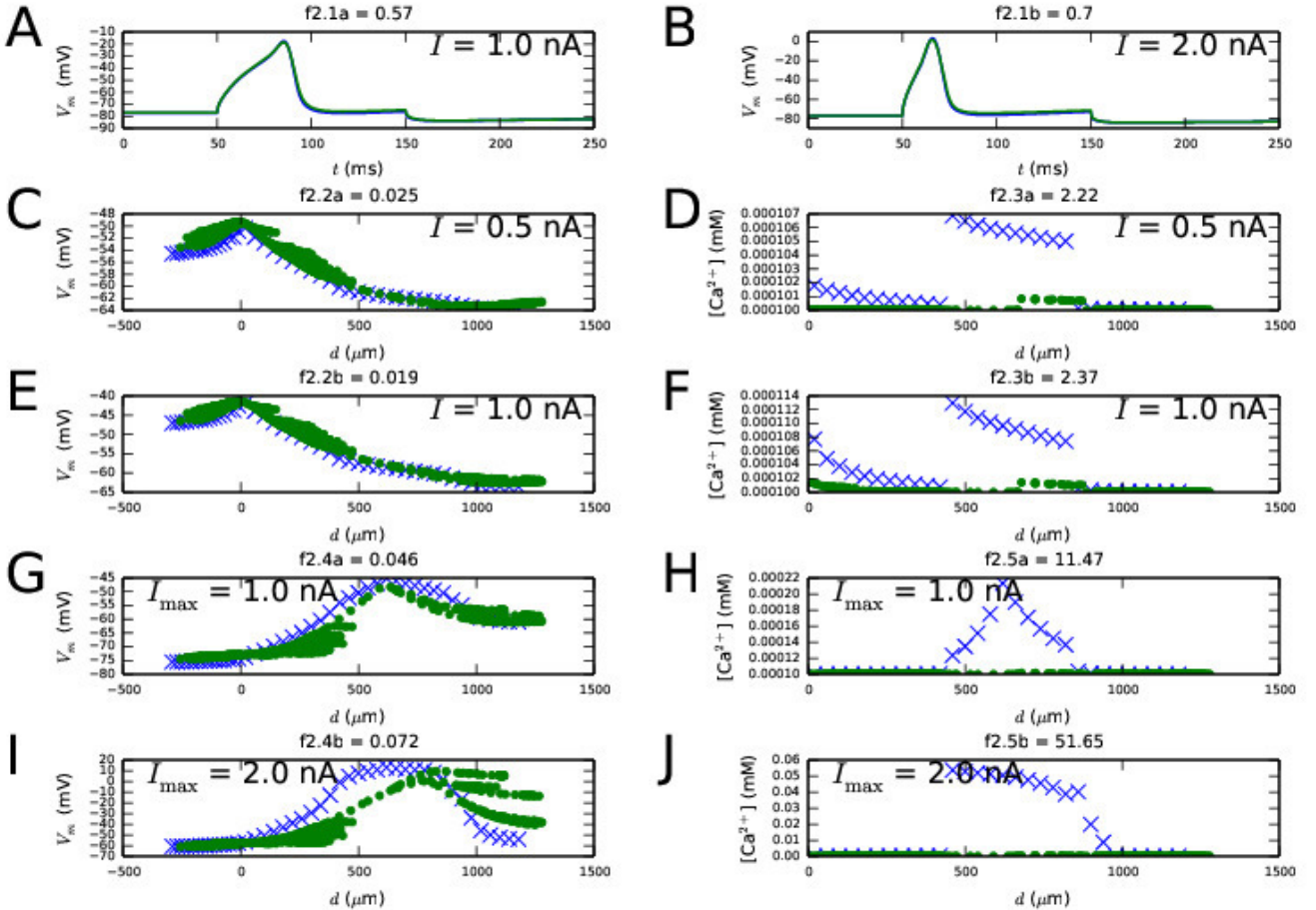

Figure S23: **Second step in the fitting of the model with reconstructed morphology**. See Figure 3 for the corresponding plots in the default four-step scheme for reduced morphology.
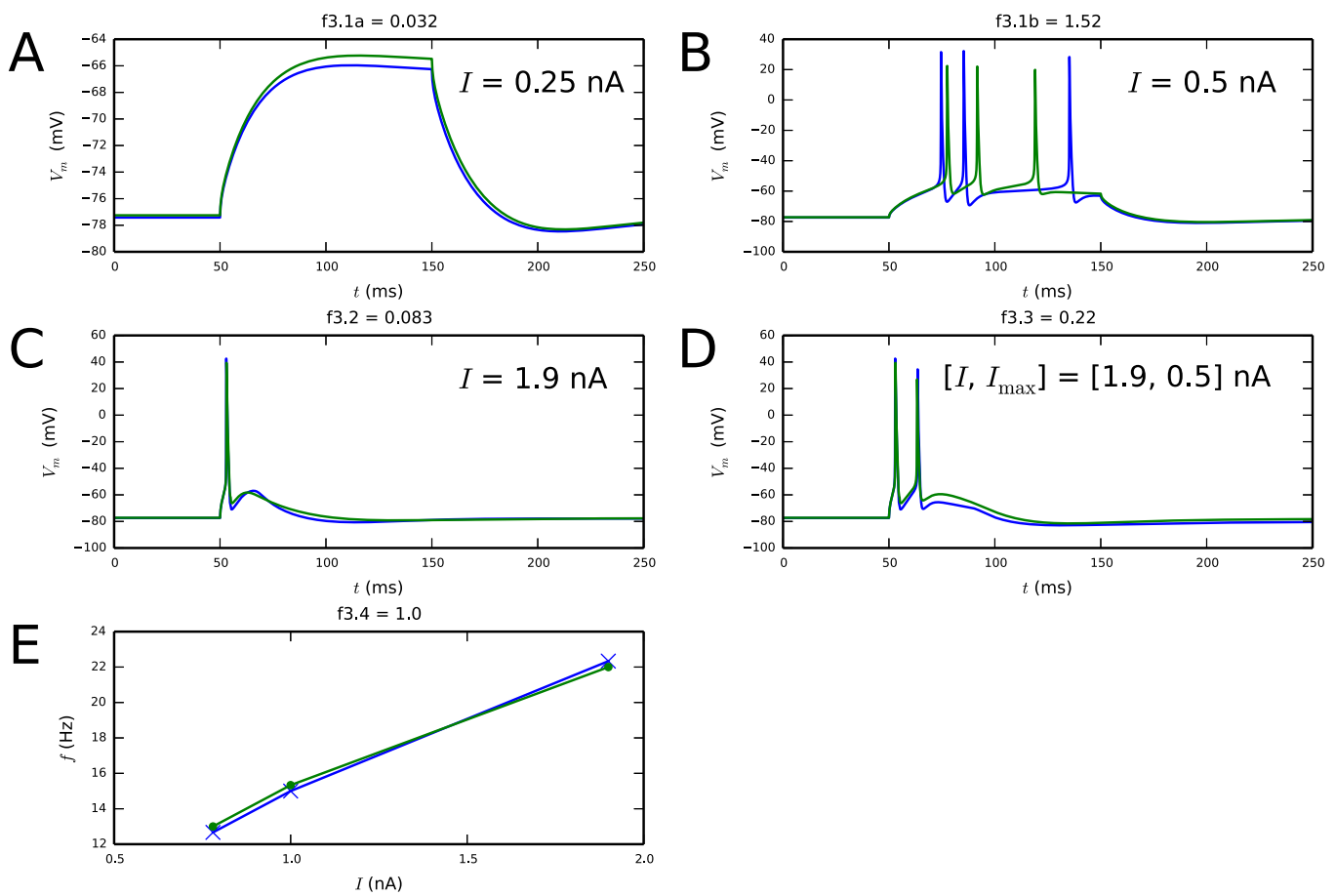
Figure S24: **Third step in the fitting of the model with reconstructed morphology**. See Figure 4 for the corresponding plots in the default four-step scheme for reduced morphology.

Table S10: **Parameter values obtained from the multi-objective optimizations of Figures S22–S24**. In these fitting tasks, the apical dendrite was divided into three sections, denoted as follows: "prox" (when the midpoint of the segment was 0–500 μm from soma), "apic" (500–800 μm), and "tuft" (further than 800 μm). See Table 3 for the corresponding parameter values obtained from the default four-stage optimization of the four-compartment model.

STEP 1			STEP 2			STEP 3	
Variable	Value		Variable	Value		Variable	Value
R_a^{soma}	284		$g_{\text{CaHVA}}^{\text{soma}}$	0.000953		$g_{\text{Nat}}^{\text{soma}}$	2.43
R_a^{basal}	88.9		$g_{\text{CaLVA}}^{\text{soma}}$	0.00172		$g_{\text{Nap}}^{\text{soma}}$	0.00593
R_a^{prox}	207		γ^{soma}	0.0005		$g_{\text{Kt}}^{\text{soma}}$	0.0369
R_a^{apic}	63		$\tau\text{decay}^{\text{soma}}$	403		$g_{\text{Kp}}^{\text{soma}}$	0
R_a^{tuft}	190		$g_{\text{SK}}^{\text{soma}}$	0.065		$g_{Kv3.1}^{\text{soma}}$	0.859
R_a^{axon}	533		$g_{\text{CaHVA}}^{\text{prox}}$	8.6e-05		g_m^{prox}	0.000207
c_m^{soma}	1.8		$g_{\text{CaLVA}}^{\text{prox}}$	0.0026		$g_{\text{Nat}}^{\text{prox}}$	0.0188
c_m^{basal}	1.76		γ^{prox}	0.00358		$g_{Kv3.1}^{\text{prox}}$	0
c_m^{prox}	1.45		$\tau\text{decay}^{\text{prox}}$	45.1		g_m^{apic}	0.000363
c_m^{apic}	3.96		$g_{\text{SK}}^{\text{prox}}$	0		$g_{\text{Nat}}^{\text{apic}}$	0.0155
c_m^{tuft}	0.851		$g_{\text{CaHVA}}^{\text{apic}}$	0.00931		$g_{Kv3.1}^{\text{apic}}$	0.0147
c_m^{axon}	1.88		$g_{\text{CaLVA}}^{\text{apic}}$	0.016		g_m^{tuft}	0
g_l^{soma}	2.36e-05		γ^{apic}	0.0138		$g_{\text{Nat}}^{\text{tuft}}$	0
g_l^{basal}	6.22e-05		$\tau\text{decay}^{\text{apic}}$	33.9		$g_{Kv3.1}^{\text{tuft}}$	0.0109
g_l^{prox}	2.64e-05		$g_{\text{SK}}^{\text{apic}}$	0.00371			
g_l^{apic}	8.35e-05		$g_{\text{CaHVA}}^{\text{tuft}}$	0.00382			
g_l^{tuft}	5.44e-05		$g_{\text{CaLVA}}^{\text{tuft}}$	0			
g_l^{axon}	5.74e-05		γ^{tuft}	0.0358			
E_h	-40.1		$\tau\text{decay}^{\text{tuft}}$	152			
g_h^{soma}	0.000374		$g_{\text{SK}}^{\text{tuft}}$	0.00291			
g_h^{basal}	0.000133						
g_h^{prox}	0.00056						
g_h^{apic}	0.00542						
g_h^{tuft}	0.00615						

S10 Division of each compartment into five segments gives an acceptable accuracy

The reduced-morphology neuron model fitting (Figures 1–4) was carried out using a dense compartmentalization, namely 20 segments per compartment. In this section, we studied the effect of numbers of segments on the accuracy of the spiking behavior. Figure S25 shows that using five segments was enough for producing the correct numbers of spikes and membrane activation statistics as responses to different stimuli, including the BAC-firing protocol. By contrast, using fewer segments gave less accurate results: With three to four segments, the validation also failed for BAC-firing inter-spike interval length (panel I), and with one to two segments, the whole BAC-firing was abolished and the neuron responded with only one spike to the applied combination of stimuli (data not shown).

S11 Simulations of pharmacological blockades reveal the contributors to the network oscillations

In this section, we carried out the simulations of spontaneous network activity (see Figure 9A–C) such that one of the ion channel types were completely blocked. Figure S26 shows the power spectrum of the population spike trains from these simulations. Similarly as in Figure 9, Figure S26 shows that in most cases the power of delta-range frequencies was elevated in comparison to corresponding Poisson process statistics. It can be observed that blocking the K$^+$ current I_{Kt} or I_{Kp} had little effect on network firing. Blocking the fast non-inactivating K$^+$ current $I_{Kv3.1}$ radically weakened the fast AHP of the neuron, leading to widened spike shapes and accelerated activation of the slower K$^+$ currents (mainly SK current; data not shown), which led to overall decreased firing rates and smaller values of power components (note, however, that the amplitude of the frequency component at approximately 1 Hz remained elevated although other frequency components were dampened). Blocking the HCN current I_h or the persistent Na$^+$ current I_{Nap} reduced the overall network excitability and blocking the low-voltage-activated Ca^{2+} current I_{CaLVA} increased the excitability, but each of these blockades preserved the overall shape of the power spectrum. The excitatory effect of I_{CaLVA} blockade was mediated by the SK current: Whenever the Ca^{2+} currents were higher, the intracellular Ca^{2+} concentration became higher as well, and thus the SK currents as well. This was most evident in blocking high-voltage-activated Ca^{2+} current I_{CaHVA}, which had almost as radical effect as blocking the SK current: the network entered a high-activity regime, and the amplification of delta-range frequencies with respect to corresponding Poisson processes vanished. Blocking the transient Na$^+$ current I_{Nat} completely abolished the spiking behavior and is therefore not shown.
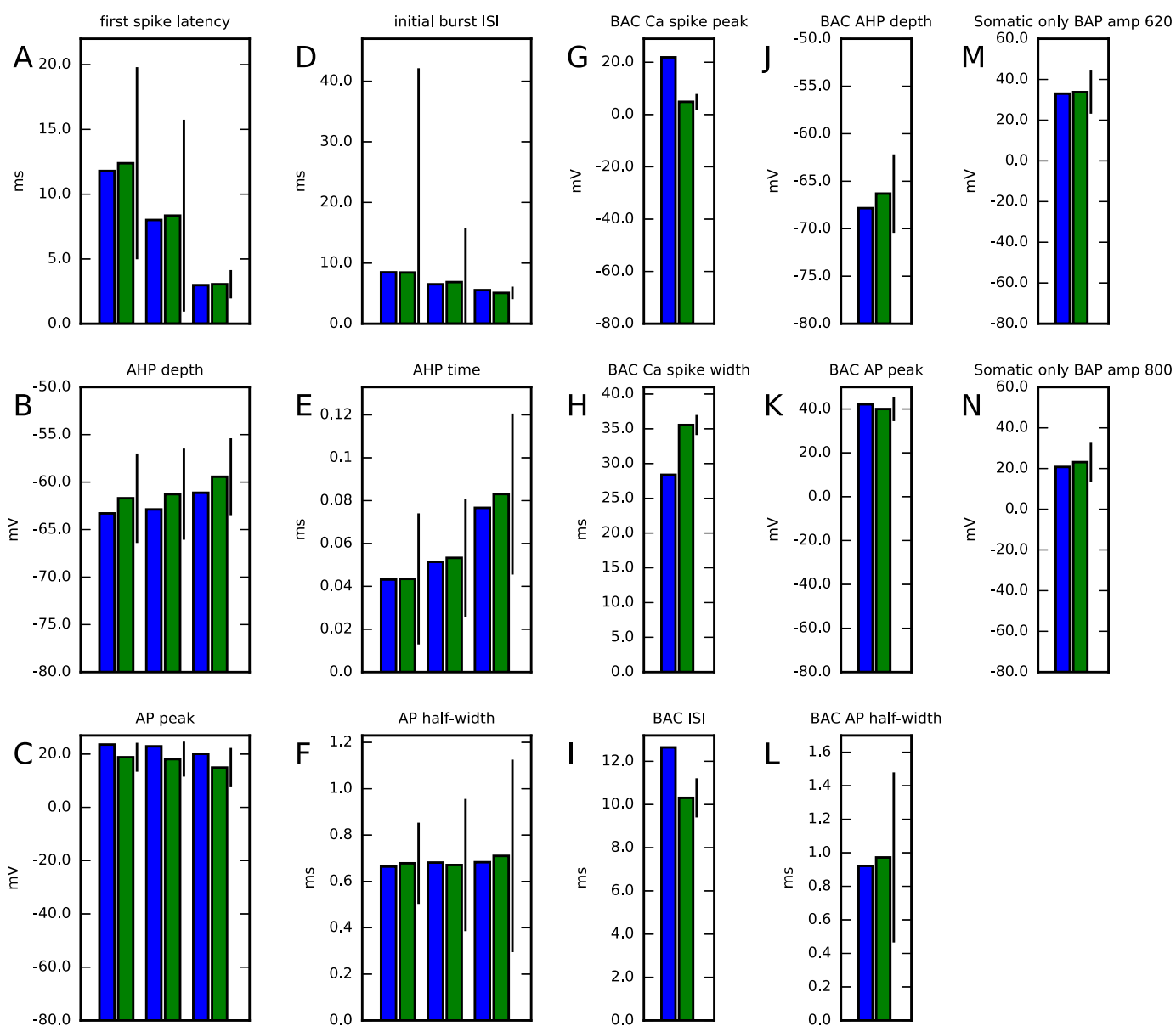
Figure S25: **Validation of the reduced model with lower-resolution spatial compartmentalization against data from full model**. Panels **A–F** show the reduced (blue) and full (green) model cell responses to a somatic DC. In the simulation of the reduced model, each compartment was divided into five segments (see Figure 7 for comparison with simulations using 20 segments). The bar represents the SD in the corresponding experimentally measured quantities. The values shown correspond to three different simulations, where the DC amplitudes were 0.78, 1.0 and 1.9 nA. Panels **G–L** show the responses to stimuli that induce BAC firing, i.e., a combination of a square pulse of duration 5 ms and amplitude 1.9 nA and an EPSP-like stimulus at the apical dendrite, separated by a 5-ms delay (somatic stimulus comes first). Panels **M–N** show the membrane-potential responses to a tonic, somatic stimulus-induced spike at distant apical dendrite.
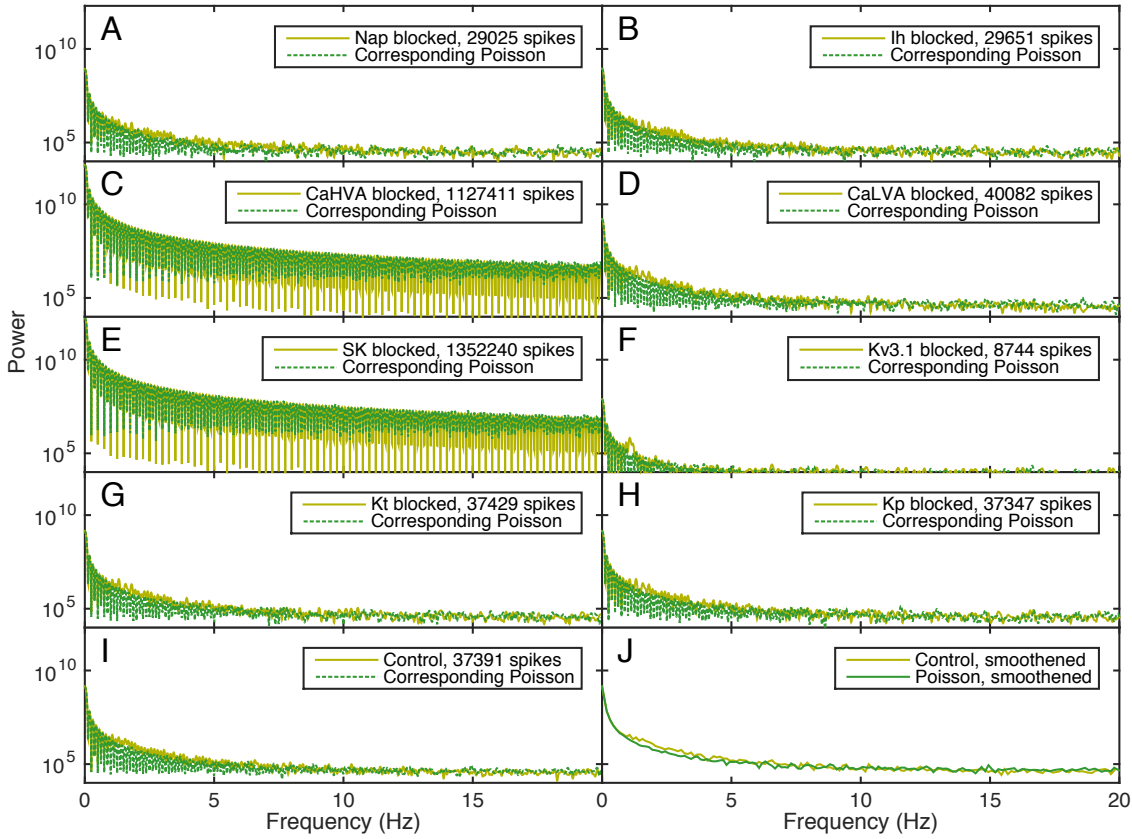
Figure S26: **Population spike train power spectra in simulations of complete blockade of different ion channels**. The yellow curves in the Panels A–I show the power spectra of the population spike train obtained from simulations of 1000 neurons, where one ion channel type is blocked in each panel (compare with Figure 9A–C, intra-network connection weight 0.21). The green dashed curves show the power spectra of the corresponding Poisson processes (the λ term fitted to give the same number of events as spikes in the network simulation). **A**: Persistent Na$^+$ current blocked. **B**: HCN current blocked. **C**: HVA Ca^{2+} current blocked. **D**: LVS Ca^{2+} current blocked. **E**: Ca^{2+}-activated K$^+$ current blocked. **F**: Kv3.1 current blocked. **G**: Transient K$^+$ current blocked. **H**: Persistent K$^+$ current blocked. **I**: Control network — the same data were shown in Figure 9C. **J**: The curves show the local maxima of the frequency spectra of the control network in panel I.

S12 Network simulations with different connectivity patterns reveal but small effects on network responses to oscillations

We applied the Watts-Strogatz model [S8] of network connectivity to produce network topologies that lie on a continuum between random (in the Erdős-Rényi sense) and locally connected networks. We first set the $N = 150$ nodes of the network in a ring, and for each node, drew a connection from n nearest neighbors, where n was picked from a binomial distribution $\text{Bin}(N, p)$ with connection probability 0.125. This resulted in the same average connectivity as the procedure used in [S9] and in the experiments of Figures 8 and 9. We also weighted each connection with an additional factor 1.24, which gave the same average synaptic drive as the procedure of [S9] where unidirectional connections had a weight 1.0 and bidirectional connections a weight 1.5. Then, each connection was rewired with a probability q such that the source node was randomly picked among all nodes except the node itself. Afterwards, the network simulation was run using this connectivity pattern in a similar fashion as the simulations of Figure 9D–G. The model parameters were kept the same, except for the intra-network synaptic weights, which were set to 1.25 (i.e., 1.25×1.24 due to the abovementioned unification of unidirectional and bidirectional connections) as in the experiments of Figure 8. Figure S27 shows the network responses to oscillations of different frequencies in a similar manner as Figure 9G (i.e., the amplitude of the power component corresponding to the frequency component of the input frequency plotted against the input frequency), now using Watts-Strogatz connectivity with five different values of rewiring probability ($q = 10^{-4}$, $q = 10^{-3}$, $q = 10^{-2}$, $q = 0.1$, $q = 0.3$, and $q = 0.7$). As expected, the networks with largest rewiring probability ($q = 0.3$) were closest to the results of Figure 9G (shown with red dashes in Figure S27), but also other networks show the same shape of response curve: The mean responses of the random networks were in most cases within one SD of the responses of the Watts-Strogatz networks.
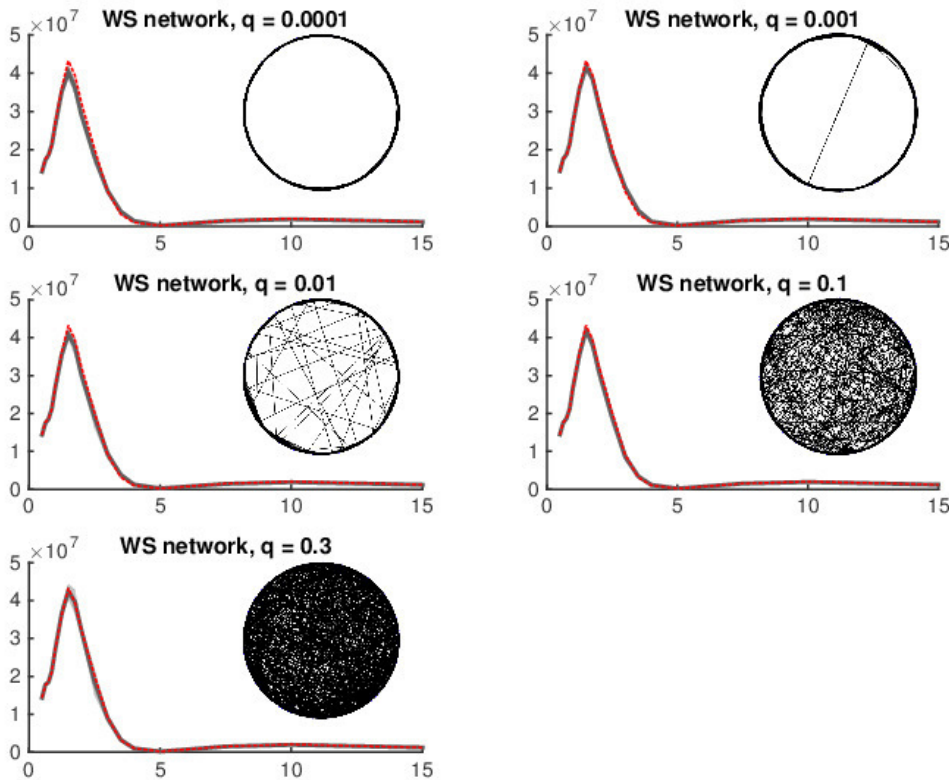

Figure S27: **The model predicts amplified L5PC network responses to delta-range oscillations in Watts-Strogatz networks.** Power amplitude of the frequency component corresponding to the background input frequency, plotted against the background input frequency. Five different values of rewiring probability were used, namely, $q = 10^{-4}$ (top-left), $q = 10^{-3}$ (top-right), $q = 10^{-2}$ (middle-left), $q = 0.1$ (middle-right), and $q = 0.3$ (bottom). The dark gray lines show the mean amplitude of the power component, while the light gray area shows the magnitude of the SD, sample size 5. The red dashed line shows the data of Figure 9G. The insets show an example network connectivity of the Watts-Strogatz network with the corresponding rewiring probability. See Figure 9D–G for details on network simulation.

References

S1. Etay Hay, Sean Hill, Felix Schürmann, Henry Markram, and Idan Segev. Models of neocortical layer 5b pyramidal cells capturing a wide range of dendritic and perisomatic active properties. *PLoS Computational Biology*, 7:e1002107, 2011.

S2. Eckart Zitzler and Simon Künzli. Indicator-based selection in multiobjective search. In *International Conference on Parallel Problem Solving from Nature*, pages 832–842. Springer, 2004.

S3. Werner Van Geit, Michael Gevaert, Giuseppe Chindemi, Christian Rössert, Jean-Denis Courcol, Eilif B Muller, Felix Schürmann, Idan Segev, and Henry Markram. Bluepyopt: Leveraging open source software and cloud infrastructure to optimise model parameters in neuroscience. *Frontiers in Neuroinformatics*, 10, 2016.

S4. Arnaud Liefooghe, Laetitia Jourdan, Matthieu Basseur, El-Ghazali Talbi, and Edmund K Burke. Metaheuristics for the bi-objective ring star problem. In *European Conference on Evolutionary Computation in Combinatorial Optimization*, pages 206–217. Springer, 2008.

S5. Armin Bahl, Martin B Stemmler, Andreas VM Herz, and Arnd Roth. Automated optimization of a reduced layer 5 pyramidal cell model based on experimental data. *Journal of Neuroscience Methods*, 210(1):22–34, 2012.

S6. Srikanth Ramaswamy and Henry Markram. Anatomy and physiology of the thick-tufted layer 5 pyramidal neuron. *Frontiers in Cellular Neuroscience*, 9:233, 2015.

S7. Mara Almog and Alon Korngreen. A quantitative description of dendritic conductances and its application to dendritic excitation in layer 5 pyramidal neurons. *Journal of Neuroscience*, 34(1):182–196, 2014.

S8. Duncan J Watts and Steven H Strogatz. Collective dynamics of 'small-world'networks. *Nature*, 393(6684):440–442, 1998.

S9. Etay Hay and Idan Segev. Dendritic excitability and gain control in recurrent cortical microcircuits. *Cerebral Cortex*, 25(10):3561–3571, 2015.